# A laboratory and theoretical study of the boundary layer adjacent to a vertical melting ice wall in salt water

By EDWARD G. JOSBERGER†

AND SEELYE MARTIN

Department of Oceanography WB-10, University of Washington,
Seattle, WA 98195

In an experimental and theoretical study we model the convection generated in the polar oceans when a fresh-water ice wall melts in salt water of uniform far-field temperature $T_\infty$ and salinity $S_\infty$. Our laboratory results show that there are three different flow regimes which depend on $T_\infty$ and $S_\infty$. First, when $T_\infty$ and $S_\infty$ lie between the maximum density curve and the freezing curve, the flow is only upward. Secondly, for the oceanic case $30 \leqslant S_\infty \leqslant 35\%$ and $T_\infty < 20\,^\circ\text{C}$, the flow consists of a laminar bidirectional flow at the bottom of the ice and a turbulent upward flow along the remainder of the ice wall. The laminar flow consists of an upward flowing layer approximately 2 mm thick inside of a downward flowing outer layer approximately 10 mm thick. Thirdly, for the same range of $S_\infty$ but for $T_\infty > 20\,^\circ\text{C}$, the flow reverses: at the top of the ice there is a laminar bidirectional flow above a downward turbulent flow. To model the turbulent upward flow theoretically, we numerically solve the governing equations in similarity form with a spatially varying eddy diffusivity that depends on the density difference between the ice-water interface and the far-field. The laboratory data then allows us to evaluate the dependence of eddy diffusivity on $T_\infty$ and $S_\infty$. The results show that the magnitude of the eddy diffusivity is of the same order as the molecular viscosity and that both mass injection at the interface and opposed buoyancy forces must be included in a realistic flow model. Finally, we use an integral approach to predict the far-field conditions that yield the high-temperature flow reversal and obtain a result consistent with our observations.

## 1. Introduction

Vertical ice walls in the world ocean occur for both sea and glacier ice. For first and multi-year sea ice, which at the beginning of the melt season have salinities less than 4‰, the vertical length scales range from 0·5 to 4 m. For glacier ice or icebergs, the vertical length scales are typically 100 m for the North Atlantic icebergs, and 250 m for the Antarctic icebergs. For sea ice, melting occurs during the polar summer for ice floating in seawater which is warmed above its freezing point by solar radiation. For icebergs, melting occurs throughout the year once the icebergs are advected into seawater with temperatures above freezing.

Because of the difficulty in doing field measurements near large ice masses and at the ice edge, investigators use laboratory experiments to understand the melt-driven convection. Two different physical phenomena complicate this convection; the

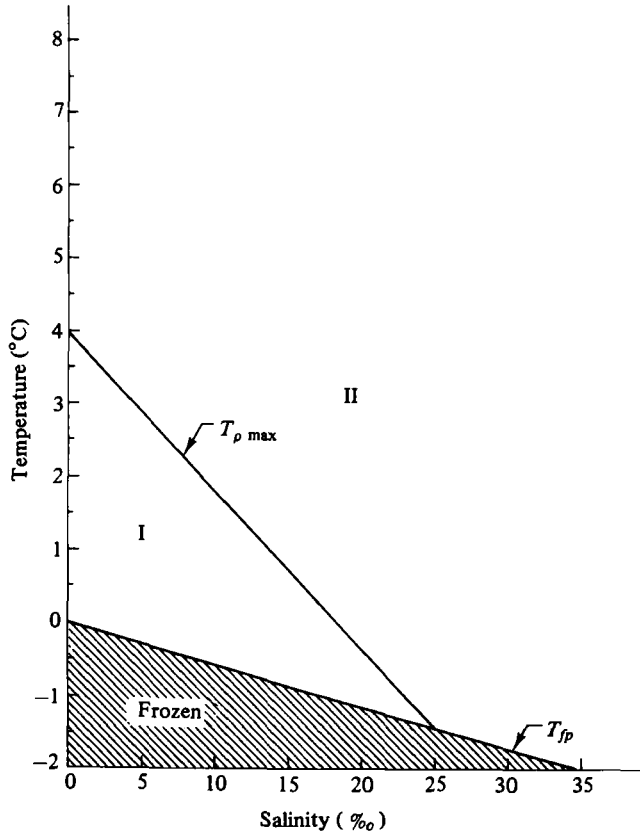† Present address: Ice Dynamics Project, U.S. Geological Survey, University of Puget Sound, Tacoma, WA 98416.

FIGURE 1. A $T$–$S$ diagram for salt-water solutions showing the location of the freezing-point depression line $T_{fp}$, and the maximum density line $T_{\rho max}$. See text for further discussion.

existence of low-temperature density maxima for fresh and salt water, and the much lower diffusivity of salt compared with heat. For the first case, figure 1 shows how the position of the maximum density line, $T_{\rho max}$, and the freezing-point depression line, $T_{fp}$, divide the temperature–salinity ($T$–$S$) diagram for salt-water solutions into two parts. The maximum density line comes from the equation of state for sea water derived by Gebhart & Mollendorf (1977), while the freezing line comes from Weast (1977). For $S < 35\%_0$, the freezing-point depression temperature $T_{fp}$ is nearly linear, and can be written as
$$T_{fp} = -mS, \tag{1}$$
where $m = 0 \cdot 060 \, °C \, \%_0^{-1}$.

   On figure 1, dilution of salt water with fresh water at the same temperature always produces less dense water because the coefficient of saline expansion
$$\beta = \frac{1}{\rho} \frac{\partial \rho}{\partial S}, \tag{2a}$$
where $\rho$ is density, is always positive. Cooling, however, produces either less or more dense water, depending on whether $T$ and $S$ fall respectively in region I or II. At the maximum density line, the coefficient of thermal expansion
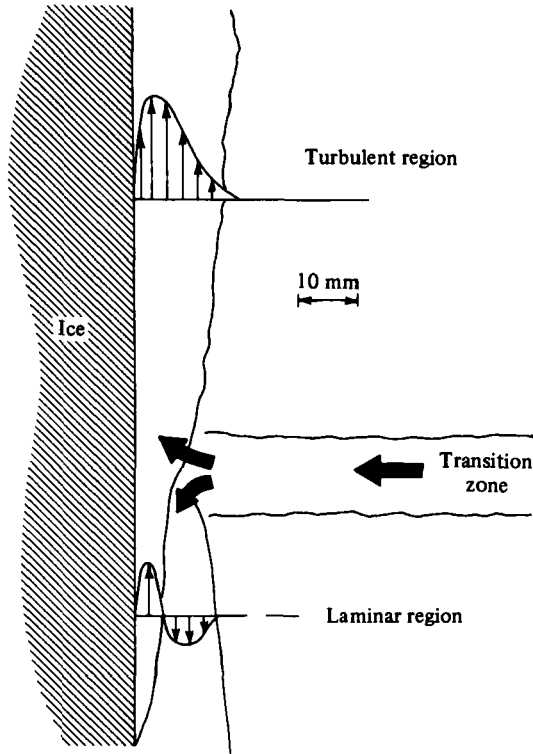$$\alpha = \frac{1}{\rho} \frac{\partial \rho}{\partial T} \tag{2b}$$

FIGURE 2. A sketch of the observed flow next to the ice for $T_\infty < 20\,°C$ and $30 < S_\infty < 35\%_0$.

changes sign. When $T$ and $S$ lie in region I, cooling and dilution produce reinforcing upward buoyancy forces. When $T$ and $S$ lie in the oceanographically interesting case of region II, cooling and dilution produce opposing buoyancy forces.

The present study shows that three different convective boundary layers form adjacent to a vertical ice wall, dependent on the values of the far-field temperature $T_\infty$ and salinity $S_\infty$ of the surrounding fluid, and on the thermal driving $T_d$ defined as

$$T_d = T_\infty - T_{fp}(S_\infty), \qquad (3)$$

where $T_{fp}(S_\infty)$ is the far-field freezing point. The thermal driving is a convenient parameter with which to characterize our experiments because it is only a function of the far-field conditions and hence independent of the unknown ice–water interface temperature and salinity.

Depending on the values of $T_\infty$, $S_\infty$, and $T_d$, we obtain the following three flows. First, when $T_\infty$ and $S_\infty$ lie in region I, we observe a simple convective boundary layer whose thickness increases from the ice bottom. Secondly, when $T_\infty$ and $S_\infty$ lie in region II and for $T_d < 20\,deg$ both a laminar and turbulent boundary layer form. This flow which is sketched in figure 2, consists of a laminar upward flowing layer inside of a downward flowing layer both below an upward flowing turbulent layer. Dilution drives the inner laminar flow and the turbulent flow while cooling drives the outer laminar flow. Thirdly, for $T_\infty$ and $S_\infty$ in region II and $T_d > 20\,deg$, the entire flow reverses, so that a bidirectional laminar layer forms at the top of the ice above a downward-flowing turbulent layer.

There are three previous pertinent laboratory studies of vertical ice walls melting in warm water. First, Sandstrom (1919) placed ice blocks in a tank of seawater to model the circulation driven by melting ice sheets during the spring in both the North Atlantic Ocean and Norwegian fjords. The far-field conditions of Sandstrom's experiments lie in region II of figure 1; for this case he describes a flow adjacent to his vertical ice face similar to that shown in figure 2. Second, Bendell & Gebhart (1976) measured the heat transfer to a vertical ice wall submerged in fresh water of uniform $T_\infty$ for cases with $T_\infty$ both above and below the 4 °C density maximum. Because of the density maximum, a bidirectional flow may occur for $T_\infty$ between 4 °C and 8 °C. From temperature observations, they inferred the flow was upward for $T_\infty < 5\cdot6$ °C and downward for warmer temperatures. From measurement of the weight change of the ice blocks, Bendell & Gebhart found the heat transfer to be a minimum at 5·5 °C. Third, Huppert & Turner (1978) investigated the effect of a linear salt gradient at 20 °C on the convection; they found that the melting generated a nearly horizontal, layered convection pattern where each layer had a thickness of order 10 millimetres.

There are also numerous laboratory, theoretical and numerical studies of the convection adjacent to a vertical wall driven by the diffusion of either single or multiple species. Gebhart & Pera (1971) and Josberger (1979) summarize the pertinent work.

The present paper, following a brief discussion of the non-dimensional parameters in §2, describes in §3 a series of laboratory experiments where vertically-oriented blocks of freshwater ice melt in salt water for a variety of uniform far-field temperatures and salinities. Then after discussion of the experimental results in §4, §5 presents a model of the turbulent boundary layer, and §6 contains the discussion of the numerical solution of the governing equations. Finally, §7 describes an integral approach to the prediction of the high-temperature flow reversal, then compares the predicted reversal with the experimental results.

## 2. Boundary-layer parameters

For a laminar boundary layer adjacent to a flat plate, the magnitudes of the Prandtl number $Pr$, the Schmidt number $Sc$, and the Lewis number $Le$ determine the relative thicknesses of the velocity, thermal and saline boundary layers (cf. Schlichting 1960). If $\delta_u$, $\delta_H$ and $\delta_S$ are the boundary-layer thicknesses for velocity, heat and salt, then

$$\frac{\delta_H}{\delta_u} \simeq Pr^{-\frac{1}{3}} \simeq 0\cdot3, \tag{4a}$$

$$\frac{\delta_S}{\delta_u} \simeq Sc^{-\frac{1}{3}} \simeq 0\cdot02 \tag{4b}$$

and

$$\frac{\delta_S}{\delta_H} \simeq Le^{-\frac{1}{3}} \simeq 0\cdot07; \tag{4c}$$

with the kinetic viscosity $\nu = 1\cdot8 \times 10^{-6}$ m²s$^{-1}$, the thermal diffusivity $\kappa = 1\cdot44 \times 10^{-7}$ m²s$^{-1}$ from Neumann & Pierson (1966), and the saline diffusivity $D = 6\cdot3 \times 10^{-10}$ m² s$^{-1}$, from Caldwell (1974).

The much greater size of $\delta_S$ compared with $\delta_H$ given by (4c) shows that the opposing buoyancy forces act in different regions of the velocity boundary layer $\delta_u$, which is

larger than both $\delta_H$ and $\delta_S$. The upward buoyancy dominates the inner region while the downward buoyancy dominates the outer region; this buoyancy distribution produces a bidirectional laminar flow.

Secondly, the transition to turbulence of vertical convective boundary layers depends on the magnitude of the Grashof number $Gr$, defined by

$$Gr = \frac{g(\rho_w - \rho_\infty) l^3}{\rho_\infty \nu^2}, \tag{5}$$

where $g$ is the acceleration of gravity $9 \cdot 8 \text{ m s}^{-2}$, $\rho_w$ is the water density at the ice–water interface, $\rho_\infty$ is the far-field density, and $l$ is a vertical length scale to be defined below as the length of the laminar layer. Turner (1973) in his discussion of the heated vertical wall, gives $10^9$ as the critical value of $Gr$ where the laminar flow becomes turbulent. For oceanic salinities and temperatures where significant melting occurs, $Gr$ exceeds the critical value of $10^9$ for length scales greater than $0 \cdot 5 \text{ m}$.

## 3. The laboratory experiment

In our laboratory study, the important parameters are the ambient water salinity and temperature, and the length of the ice wall. We easily model oceanic temperatures and salinities as well as 1 m vertical length scales in our experimental tank; for oceanic purposes we assume these results may be extrapolated to length scales greater than 1 m.

As figure 3(a) shows, the experiments took place in a clear acrylic tank that measured $0 \cdot 45 \text{ m}$ wide, $1 \cdot 2 \text{ m}$ long, and $1 \cdot 25 \text{ m}$ deep, which when filled contained approximately 650 kg of a sodium chloride solution. To measure the solution salinity, we used both an American Optical and an Endeco refractometer, which were respectively accurate to $1 \cdot 0\%_0$ and $0 \cdot 2\%_0$. The tank was located in a cold room; we controlled the water temperature by setting the room temperature to the desired value.

The ice used in the experiments consisted of sheets of bubble-free ice frozen around an instrument array described below. The ice sheets measured approximately $0 \cdot 2 \text{ m}$ wide, $0 \cdot 1 \text{ m}$ thick, and varied in length from $0 \cdot 5$ to $1 \cdot 2 \text{ m}$. We grew the bubble-free ice in an insulated tank measuring $0 \cdot 4 \times 0 \cdot 6 \text{ m}$ in cross-section and $0 \cdot 4 \text{ m}$ deep that had a cold plate on the bottom and two laboratory stirring motors mounted on the top. As the ice grew, the water motion created by the stirring motors swept away the air bubbles that formed at the ice–water interface. When the ice thickness grew to half the desired value or 50 mm, the array was placed in the tank so that the ice froze around it. When the ice thickness reached 100 mm, we increased the cold plate temperature to $+2 \,^{\circ}\text{C}$; the subsequent small amount of melting freed the ice from the tank bottom so that the ice was easily removed. To obtain $1 \cdot 2 \text{ m}$ long ice, we butted two $0 \cdot 6 \text{ m}$ long lengths of ice together in a cold room at $-15 \,^{\circ}\text{C}$ while slowly pouring water at $0 \,^{\circ}\text{C}$ into the joint. For this case the upper $0 \cdot 6 \text{ m}$ of the ice contained the array. Finally, for both long and short ice slabs, we smoothed one side of the ice with a laboratory hot plate to a surface that was planar to within 2 mm/m, and as figure 3(a) shows, bevelled the ice bottom to divert the buoyant water formed from bottom melting up the back side of the ice.

To hold the ice in the tank, a $12 \cdot 7 \text{ mm}$ diameter aluminium rod screwed into the top of the plastic array and was attached with a laboratory swivel clamp to a similar rod
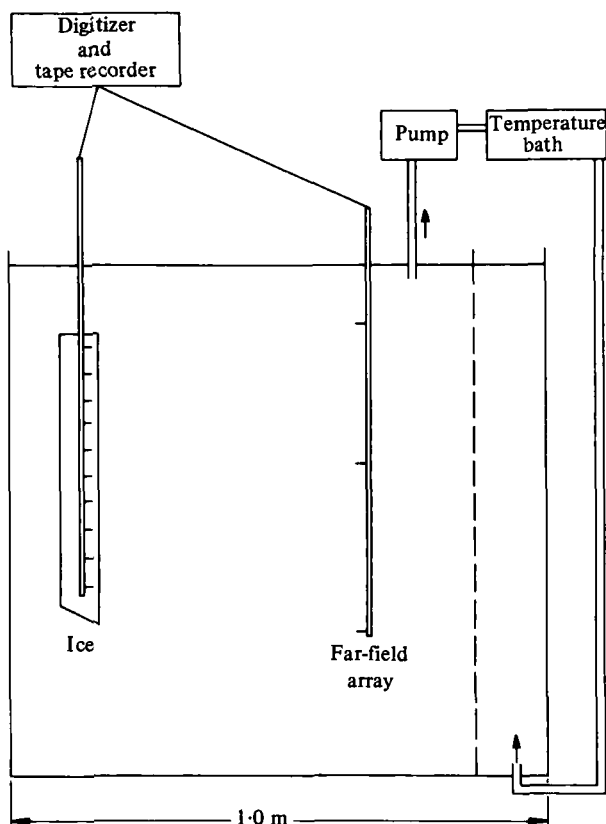
FIGURE 3. For legend see facing page.

fixed across the top of the tank. The clamp was then adjusted to bring the ice face parallel to the direction of gravity. During an experiment the vertical edges of the ice became rounded, but since the observed radius-of-curvature of the rounded edge was less than 10 mm, or much smaller than the cross-ice dimension of 200 mm; this rounding had little effect on the overall flow.

The instrument array frozen into the ice consisted of ten precision thermistors and four ablation probes mounted on a plastic support. The support measured 0·5 m long with a cross-section of 12·7 × 12·7 mm; figure 3(b) shows the arrangement of the thermistors and the ablation probes on the support. To prevent the hydrodynamic wake of one thermistor from interfering with another after the thermistors melt through, no two thermistors lay in the same vertical plane perpendicular to the ice surface. Each probe extended 15 or 20 mm beyond the plastic support so that the probes melted through the ice at different times during an experiment.Two thermistors, located at the same horizontal level, determined the horizontal variation of the interface temperature.

The thermistors were Yellow Springs Instruments precision thermistors, no. 44007, with a time constant of 1 s and a dissipation constant of 8 mW $K^{-1}$ in a well-stirred oil bath. These thermistors were roughly spherical with a 2·4 mm diameter, with their leads insulated with a 15 to 20 mm length of snug-fitting shrink tubing filled with self-curing silicone rubber. We mounted each sensor on a 5 mm wide, 1 mm thick
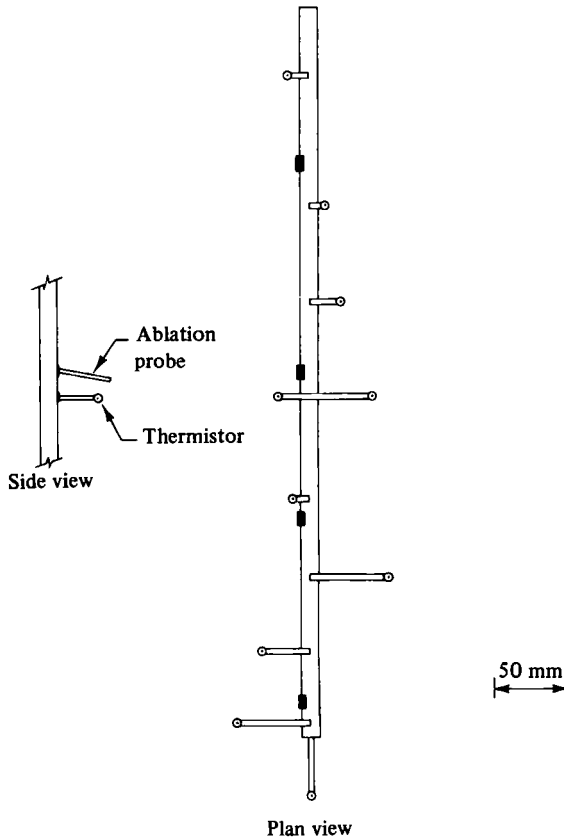
FIGURE 3. (*a*) The experimental apparatus. (*b*) The thermister array:
⊙, thermistor; ▮, ablation probe.

plastic strip of varying length, then fastened this strip to the main support at the required level.

The four ablation probes were strips of plastic rule measuring 35 mm in length and $3 \times 1$ mm in cross-section mounted on the array in a vertical plane perpendicular to the ice surface. Because the large index-of-refraction change at the interface hindered sighting directly along the ice plane we tilted the ablation probes down at a $10°$ angle. When viewed at a horizontal angle of $5°$ from the ice plane the probe and its reflected image in the ice formed an inverted V. To determine the ablation rate, we periodically measured the horizontal distance from the tip of the probe to the apex of the V with a Keuffel and Esser measuring transit, which had an accuracy of $\pm 0.25$ mm.

To measure the far-field temperature and salinity, we used an array consisting of three thermistors, identical to those frozen in the ice, and three surgical tubes. The thermistors were mounted on a $1.2$ m long, $12.7 \times 12.7$ mm plastic rod at vertical separations of $0.25$ m. To determine the far-field salinity, we drew water samples with a syringe from three tubes taped to the plastic rod such that each tube ended at one of the thermistor levels. Figure $3(a)$ shows the position of the ice and far-field array in the tank. We placed this array $0.5$ m from the ice so that the far-field array and the array within the ice spanned the same vertical distance.

During an experiment we recorded all of the thermistor resistances on magnetic tape with a Non-Linear Systems data acquisition system with a one minute scan rate. The accuracy of these measurements in temperature was $\pm 0.02$ deg. To visualize the flow, we introduced reflecting flakes made of finely-ground mother-of-pearl into the tank, then illuminated the suspension with a vertically oriented slit light source generated by a slide projector. The light entered the tank from the end near the ice slab and passed through the bubble-free ice to illuminate the flow; we viewed and photographed the flow field through the side of the tank normal to the light plane. Because the settling time of the flakes was of order days, the flakes accurately followed the convective motions. To prevent dissolution of the flakes, we made the water slightly basic by adding $0.2$ kg of sodium bicarbonate to the water.

Because the flakes rotate in the flow and thus may not be visible for the entire exposure, we also estimated the boundary-layer velocities through injection into the boundary layer of a neutrally buoyant mixture of Indian ink and salt water, then timing its motion past thermistors on the array. Also, the dye dispersion across the boundary layer gave us a thickness estimate. We obtained another thickness estimate by sighting across the boundary layer parallel to the ice surface at a Moiré grid. The large index-of-refraction change between the water near the ice and ambient water distorted the grid and made visible the edge of the boundary layer.

To maintain homogeneous far-field conditions, we relied on both the large mass of water in the tank and a pumping and heating system. Figure 3 (*a*) shows the pumping system; the colder, less saline water generated by the melting ice was pumped from the surface through a constant temperature bath, then returned to the bottom of the tank behind a perforated diffusing screen. This screen allowed the water to mix in the tank without affecting the flow next to the ice. The pumping rate was of order $100$ mm$^3$ s$^{-1}$ which produced an upward velocity in the tank of $0.15$ mm s$^{-1}$, or much less than the $10$ mm s$^{-1}$ observed boundary-layer velocities.

To summarize, a typical experiment proceeded as follows: We removed the ice from cold storage at $-15°$ C, then allowed the ice to warm to $-1$ °C. This procedure took about 30 min during which time the tank was first vigorously stirred, then allowed to come to rest to ensure homogeneous far-field conditions. We then connected the thermistors to the data acquisition system and began recording just prior to submerging the ice. Once the ice was submerged, the experiment began. During the experiment we measured the exposed lengths of the melt probes every 30 minutes and drew far-field salinity samples. We also observed and photographed the flow using reflecting flakes and dye injections. The experiment ended when the ice melted past all of the thermistors frozen in the ice. After removing the array from the tank, we rinsed the array with fresh water, then calibrated it in a crushed ice and fresh-water zero-degree bath.

## 4. The laboratory observations

The laboratory experiments cover the range of oceanic salinities and far-field temperatures up to 27 °C. In this section we first discuss the laminar and turbulent flows which occur for $T_d < 20$ deg, then the high-temperature flow reversal for $T_d > 20$ deg.

### 4.1. *The laminar unidirectional and bidirectional flow for $T_d < 20$ deg*

Along the lower portion of the ice we observed either bidirectional or unidirectional upward laminar flow, depending on the far-field conditions. As §1 describes, when $S_\infty$ and $T_\infty$ lie in the region II of figure 1, the flow is bidirectional; when $S_\infty$ and $T_\infty$ lie in region I of figure 1, the flow is unidirectional and upward. To determine the properties of the region I flow, we performed two experiments with far-field conditions

$$T_\infty = 0.05\,°C, \quad S_\infty = 14.2\%_o, \quad \text{and} \quad T_\infty = 1.8\,°C, \quad S_\infty = 8\%_o.$$

As figure 4 shows for the first experiment, in both cases an upward-flowing unidirectional boundary layer of order 10 mm thick occurred. For these experiments, table 1 lists $S_\infty$, $T_\infty$, and $T_d$, as well as both the observed $T_w$ and the values of $S_w$ from equation (1), which were vertically uniform. This uniformity suggests that a similarity solution to the governing equations will describe the observed flow.

In contrast, when $T_\infty$ and $S_\infty$ lie in region II of figure 1 the laminar velocity field is bidirectional consisting of a narrow upward inner flow next to the ice inside of a wider downward outer flow. Figure 2, a sketch, and figures 5 (*a, b*), streak photographs, show the observed flow. The two photographs show that immediately next to the ice there is an upward inner flow of order 1 mm thick which grows in thickness from the ice bottom; dye injections show the velocities in this region are of order 1 mm s$^{-1}$. Two features on each photograph mark the edge of the upward flow; the apexes of the V-shaped streak trajectories, and the region of short streaks and dots a few millimetres from the ice located between two regions of longer streaks. The arrows on the photographs point to several of the V-shaped trajectories, where the arrow shafts lie along the region of short streaks and dots. The streak trajectories suggest that water parcels move from the outer flow, through a region of no vertical motion, and into the inner flow. The photographs also show that the outer flow thickness is of order 10 mm and increases downward except near the ice bottom, where the flow constricts and curves slightly under the ice. These effects result from the absence of the wall which allows the flow to accelerate; hence through Bernoulli's law the flow narrows and curves under the ice.

In the upper third of the inner flow, we observed small-amplitude waves with horizontal crests parallel to the ice surface at the outer edge of the saline layer. These waves propagate upward with phase speeds of order 1 mm s$^{-1}$ and wavelengths of order 5 mm. The wave amplitudes grow to approximately 3 mm at which point the waves 'break' to form horizontal vortices with 3 mm diameters. Approximately 30 mm above the point at which the waves form vortices the inner flow becomes turbulent. On the ice beneath these waves and vortices, vertical grooves appear which are separated by approximately 25 mm and have a width and depth of order 1 mm. Gebhart (personal communication) attributes the groove formation to a secondary flow consisting of longitudinal rolls in the inner flow; however, we did not observe these rolls.

At the level of transition to turbulence, we observe that the turbulent diffusion transported both dilute water and upward momentum away from the ice over a horizontal distance comparable to the thermal boundary layer thickness. This upward buoyancy and momentum overwhelm the downward buoyancy such that the net result is an upward flowing turbulent boundary layer. The resultant divergence
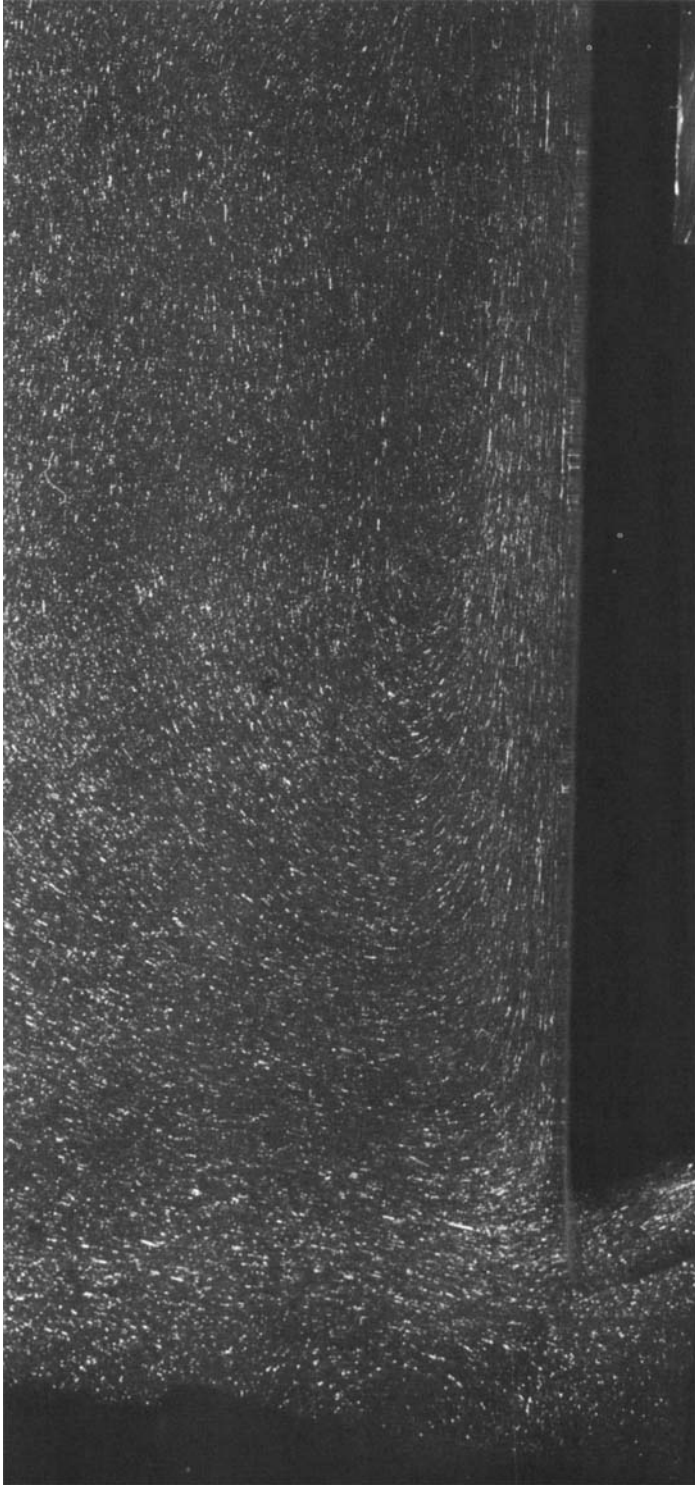
(a)

FIGURE 4. Unidirectional upward laminar flow, $T_\infty = -0.4$ °C, $S_\infty = 18$‰, 60 s exposure.

| $T_\infty$ (°C) | $S_\infty$ (‰) | $T_d$ (deg) | $T_w$ (°C) | $S_w$ (‰) |
|---|---|---|---|---|
| $+0.05$ | 14·2 | 0·78 | $-0.66$ | 12·8 |
| $+1.80$ | 8·0 | 2·50 | $-0.29$ | 5·6 |

TABLE 1. Far-field and interface conditions for the two unidirectional experiments.

between the upward turbulent flow and the downward laminar thermal flow produces a horizontal jet of ambient water flowing toward the ice. In figure 6 the jet appears as an approximately 100 mm wide horizontal band with speeds of order $1 \text{ mm s}^{-1}$. The point labelled B at the ice–water interface marks the stagnation streamline and will be called the bifurcation point. Water in the jet above the bifurcation point enters the upward turbulent flow, while water below this point enters the downward thermal flow. The streak photographs show that the velocities in the jet are much greater than the suction velocities associated with either the laminar or turbulent boundary layer.

As a result of these convective motions, the ice ablation proceeds as shown in figure 7 $(a, b)$. At the ice bottom the ablation is high, then decreases with distance upward until the bifurcation point, where the ablation abruptly increases and a notch forms in the ice. Above the notch in the turbulent regime, the ablation is greater than in the laminar regime but less than that at the bifurcation point.

Table 2 summarizes the observed properties of the laminar bidirectional flow experiments. The first four columns in the table list respectively the experiment number and the far-field conditions $T_\infty$, $S_\infty$, and $T_d$; the fifth column lists the measured length of the laminar layer $l$, which we define as the distance from the ice bottom to the bifurcation point where $l$ is not listed, we did not photograph the ice. The sixth column lists $\overline{T}_w$, which is the average of the interface temperature measurements for the laminar layer, and the seventh column lists $\bar{r}$, which is $\overline{T}_w$ divided by the far-field freezing point, or

$$\bar{r} = \overline{T}_w / T_{fp}(S_\infty). \tag{6}$$

The table shows that $\bar{r}$ decreases from near 1 when the ice is close to equilibrium with the far-field conditions to near zero for $T_d > 9$ deg. Finally, the last column lists $Gr$ from (5) for the various runs, which we compute from (1), the equation of state, and the other data in the table. The average Grashof number is $2 \times 10^8$, or an order-of-magnitude less than the critical value given by Turner (1973) for turbulent transition of natural convective flows driven by either heat or mass diffusion. Our lower value probably results from the outer downward flow that enhances the velocity shear which further destabilizes the laminar flow.

Next, figure 8 shows for each experiment the vertical variation of the unaveraged value of $r$ as a function of the distance $x$ divided by $l$. Where table 2 does not list $l$, we calculate it from the average $Gr$ and the other listed data. Examination of the figure shows that the wall temperature is coldest at the bottom then slowly increases upward with a maximum variation of 20 % for $3 \leqslant T_d \leqslant 5$ deg, corresponding to a temperature change of approximately 0·35 deg. For $T_d > 5$ deg the variation of $r$ with distance decreases because $T_w$ at any level approaches 0 °C.
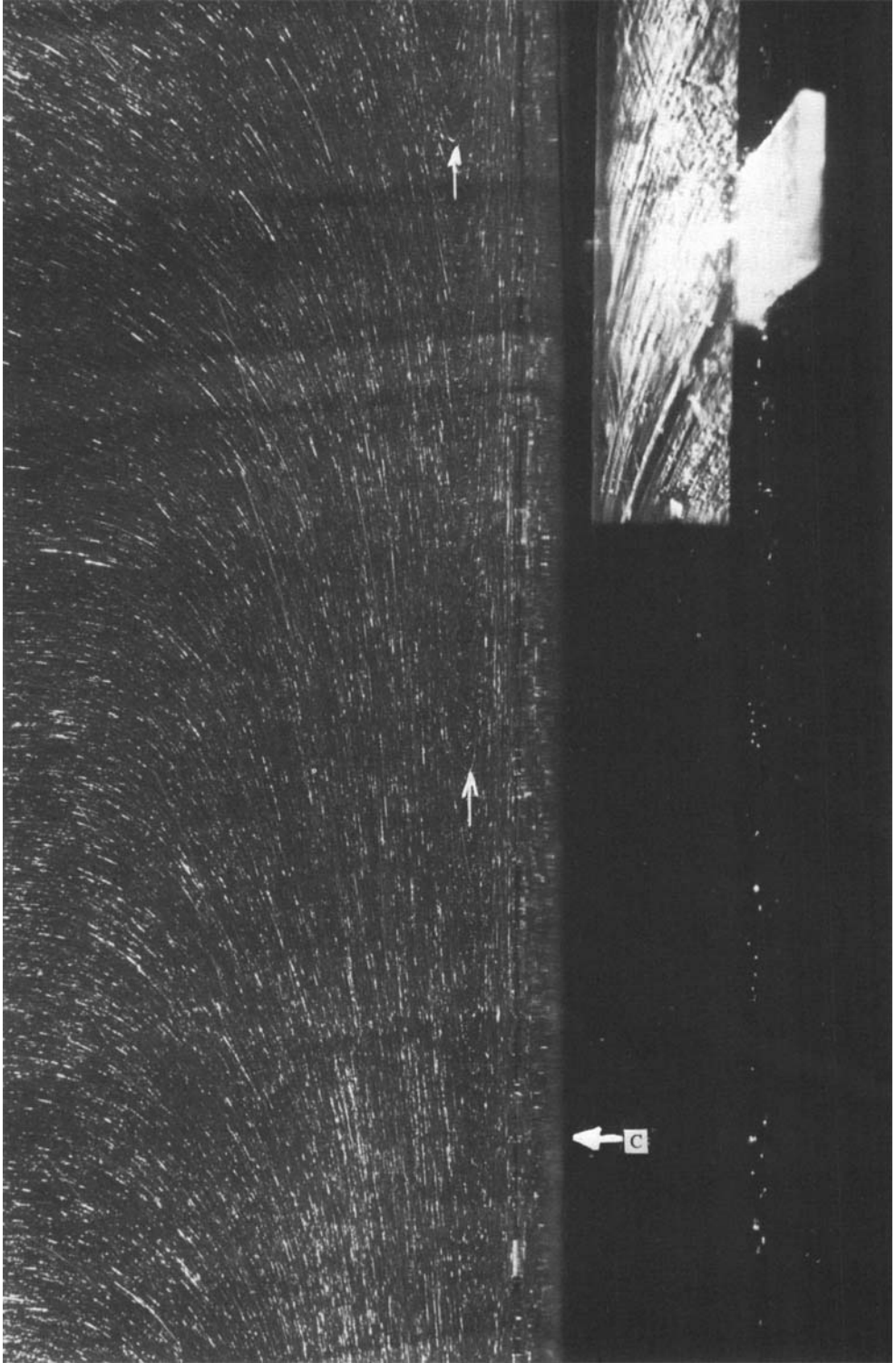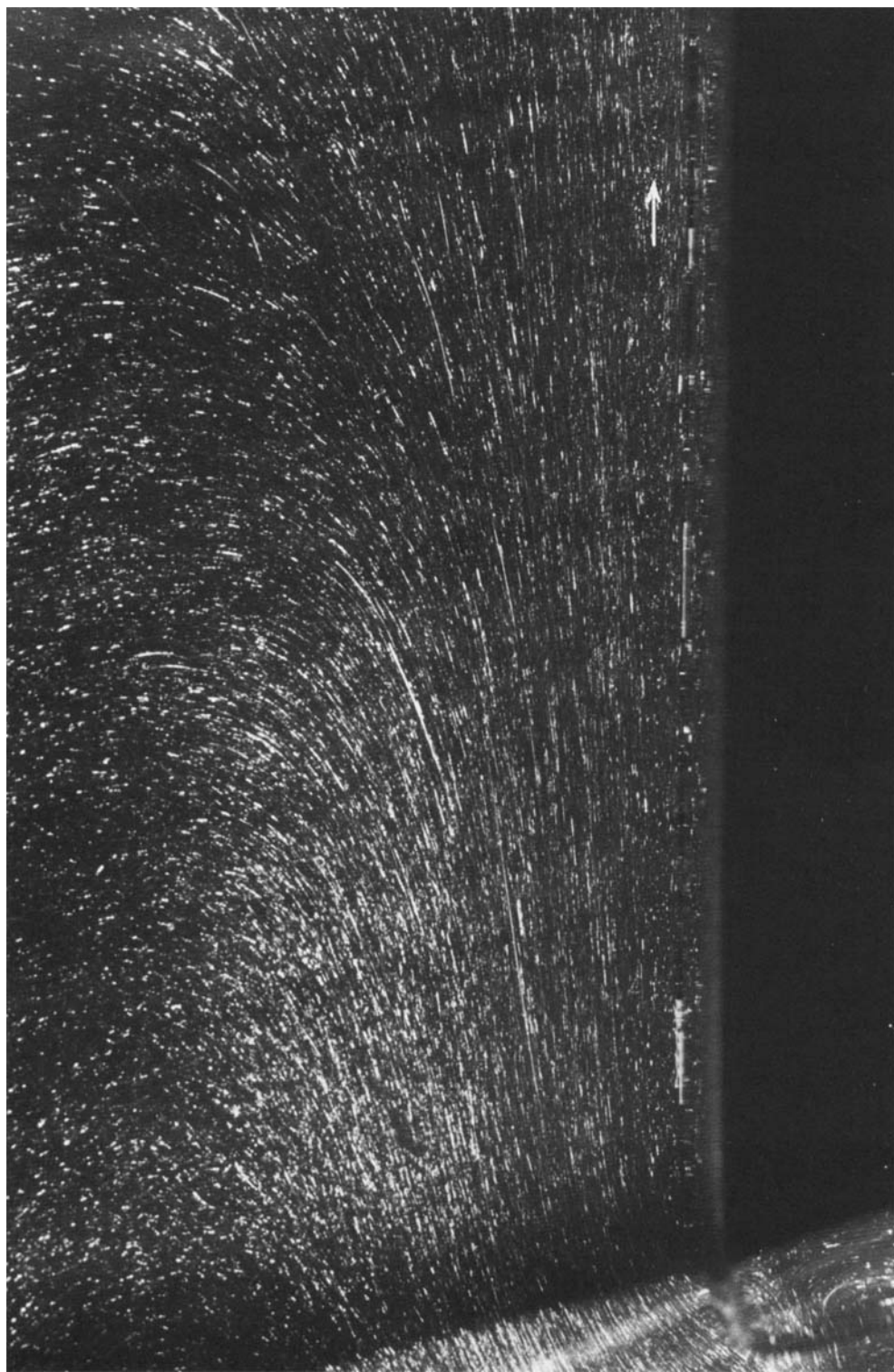
FIGURE 5(a). For legend see facing page.

(b)

FIGURE 5. Streak photographs of the bidirectional flow for $T_\infty = -1\cdot15$ °C, $S_\infty = 33\cdot0\%_0$ and a 60 s exposure. (a) The upper portion of the ice; (b) the lower part. The top of (b) joins (a) at the level marked C.
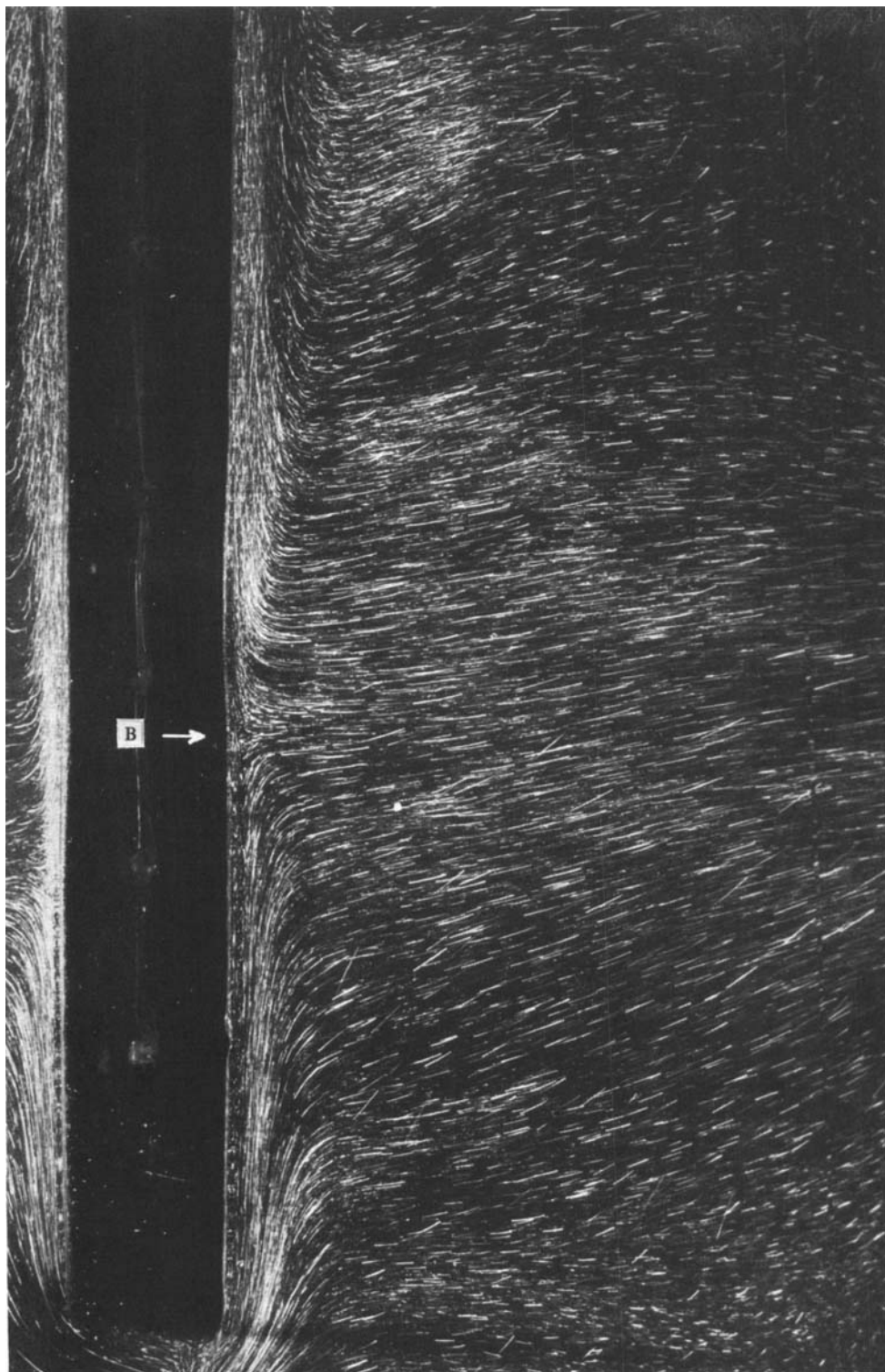
FIGURE 6. Bifurcation of the horizontal jet; the arrow labelled B marks the bifurcation point; $T^{..} = 2 \cdot 2\ ^{\circ}\mathrm{C}$; $S_{\infty} = 30 \cdot 0\ ‰$, 30 s exposure.

### 4.2. *The turbulent boundary layer above the bidirectional laminar flow*

Our observations show that the flow above the bifurcation point is only upward and turbulent. The initial thickness of the flow is 10–30 mm; the thickness also increases with distance from the bifurcation point. Dye injections show that the maximum upward velocity is of order 10 mm s$^{-1}$, located 2–3 mm from the ice, and increases with height. The dye also shows that the outer edge of the layer fluctuates toward and away from the ice with the passage of turbulent eddies.

Our thermistor records also give a qualitative description of the turbulent structure within the boundary layer. Despite the relatively large size of the thermistor beads, we assume that they give an accurate qualitative description for two reasons. First, the small thermistor response time allows the thermistors to detect some of the large temperature fluctuations in the turbulent flow. Secondly, visual observations of the flow give a description of the turbulent structure similar to that deduced from the thermistor records. Figure 9, a representative thermistor record, may be viewed as the temperature measured by a thermistor moving across the boundary layer at a speed equal to the ablation rate and it shows several features of the flow.

First, within 2 mm of the ice, no significant temperature fluctuations occur and the temperature increases monotonically. Secondly, in a region between 2 mm and 10 mm from the ice, the temperature fluctuations are as large as 0·5 deg, and the fluctuation magnitude increases with increasing distance. Thirdly, the large temperature fluctuations at the outer edge of the boundary layer result from the wavering motion of the boundary between turbulent and quiescent fluid. Lastly, the thermal boundary-layer thickness of 10 mm roughly equals the momentum boundary-layer thickness observed by dye injections.

Table 3 summarizes the observations from the turbulent flow experiments. The first four columns list the experiment number, and the far-field conditions $T_{\infty}$, $S_{\infty}$ and $T_d$. The fifth column lists $T_w$, where we found that its measured values were constant to within 0·02 deg along the interface for any particular experiment, in contrast to the laminar flow where $T_w$ increased with height. The sixth column lists $x$, which we now define as the distance above the bifurcation point at which we measured the melt rate $M$ listed in the seventh column. Finally, the last two columns list $M_0$, which is the product of $M$ and $x^{\frac{1}{4}}$, and $\bar{M}_0$, which is the average of $M_0$ for each experiment.

To discuss first the temperature data, figure 10 shows the dependence of the normalized interface temperature $r$ (see equation (6)) on $T_d$. The open squares are the observed values of $r$ for $0 \leqslant T_d \leqslant 20$ deg and the dashed line is the curve

$$r = 1 \cdot 0 - \tanh{(0 \cdot 15 T_d)}. \qquad (7)$$

The data suggest that for $T_d < 9$ deg, $r$ decreases linearly with increasing $T_d$ and for $T_d > 9$ deg, $r$ approaches zero.

To next discuss the ablation, figure 7 (*a*) shows a representative ice profile after melting for 220 min at $T_d = 3 \cdot 1$ deg and figure 7 (*b*) shows the measured melt rates from this experiment. For all experiments the ice melted as shown in figure 7 (*a*); the melt rate is greatest at the bifurcation point then slowly decreases with distance above the bifurcation point. This combination of a vertically varying melt rate and the uniform wall temperatures strongly suggests that the flow can be described by a $x^{\frac{1}{4}}$ similarity transformation. In this transformation, which §5 develops, the melt rate decreases as
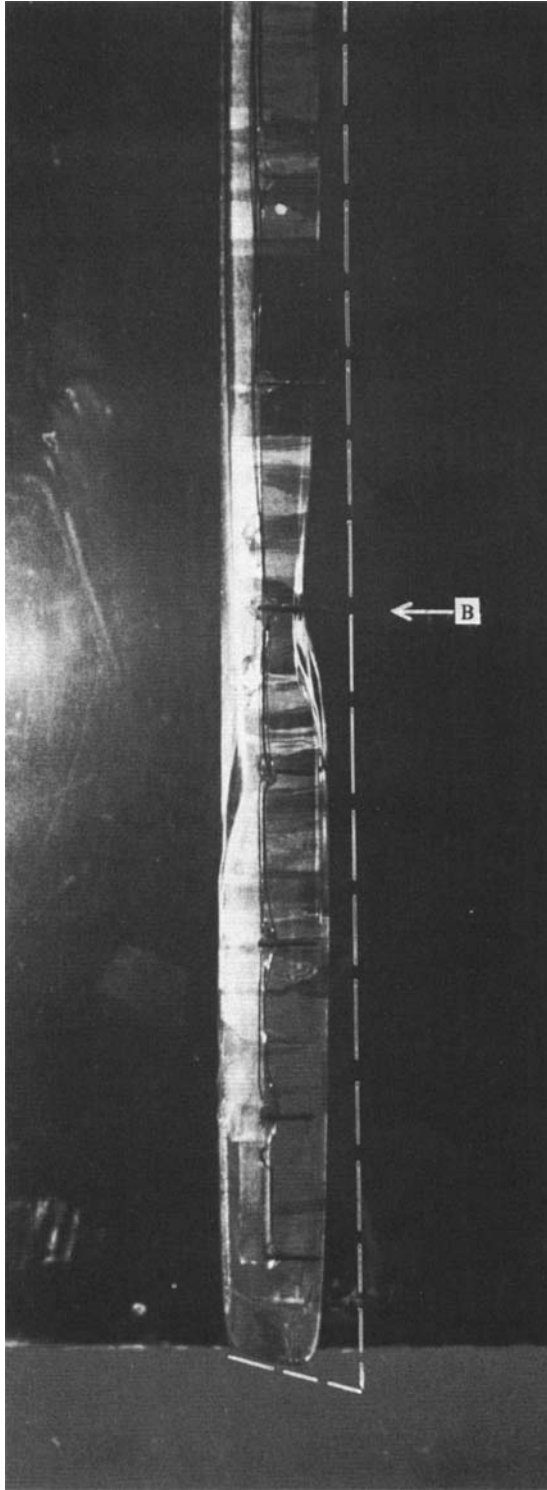
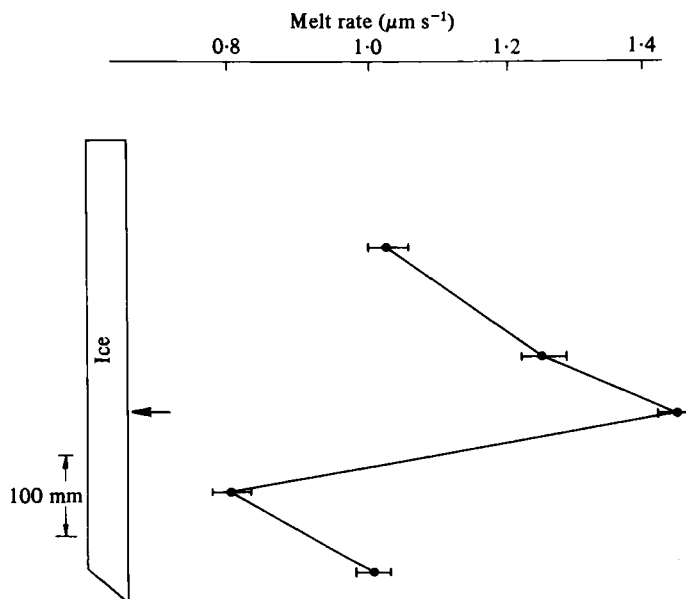FIGURE 7(a). For legend see facing page.

FIGURE 7. (a) Ice shape after melting for 220 min, $T_\infty = 1\cdot5$ °C, $S_\infty = 29\cdot0$ ‰. Dashed line indicates original ice shape. (b) Measured melt rates for the ice in (a).

| Experiment number | $T_\infty$ (°C) | $S_\infty$ (‰) | $T_d$ (deg) | $l$ (mm) | $\bar{T}_w$ (°C) | $\bar{r}$ | $Gr$ ($\times 10^{-8}$) |
|---|---|---|---|---|---|---|---|
| 1 | $-0\cdot5$ | 29·0 | 1·08 | — | $-1\cdot53$ | 0·88 | — |
| 2 | $-0\cdot72$ | 33·7 | 1·13 | 260 | $-1\cdot81$ | 0·90 | 1·5 |
| 3 | 0·0 | 29·0 | 1·65 | 300 | $-1\cdot49$ | 0·86 | 2·8 |
| 4 | 1·55 | 29·0 | 3·13 | 270 | $-1\cdot11$ | 0·64 | 5·1 |
| 5 | 2·20 | 30·0 | 3·83 | 180 | $-0\cdot97$ | 0·54 | 2·0 |
| 6 | 2·70 | 29·0 | 4·28 | — | $-0\cdot80$ | 0·46 | — |
| 7 | 2·66 | 34·4 | 4·55 | 155 | $-1\cdot03$ | 0·50 | 1·6 |
| 8 | 6·85 | 34·0 | 8·71 | 110 | $-0\cdot32$ | 0·16 | 0·2 |

TABLE 2. Properties of the laminar bidirectional experiments, see text for further description.

$x^{-\frac{1}{4}}$. To check this hypothesis, the eighth column in table 3 lists the observed $M$ multiplied by $x^{\frac{1}{4}}$. Examination of this column shows that, except for experiments 4 and 5 where $M_0$ varies by 20%, $M_0$ is constant to within 8%. If we assume that this large variation in $M_0$ for experiments 4 and 5 is caused by preferential melting around the melt probes, then the data supports the hypothesis that $M$ has a $\frac{1}{4}$-power dependence on $x$.

Figure 10 also gives the melt rate data where the circles are the observed values of $\bar{M}_0$ and the solid line is discussed below. Examination of the figure shows that the dependence of $\bar{M}_0$ on $T_d$ changes from a non-linear to a linear dependence in the vicinity of 9 deg. For $T_d \leqslant 9$ deg,

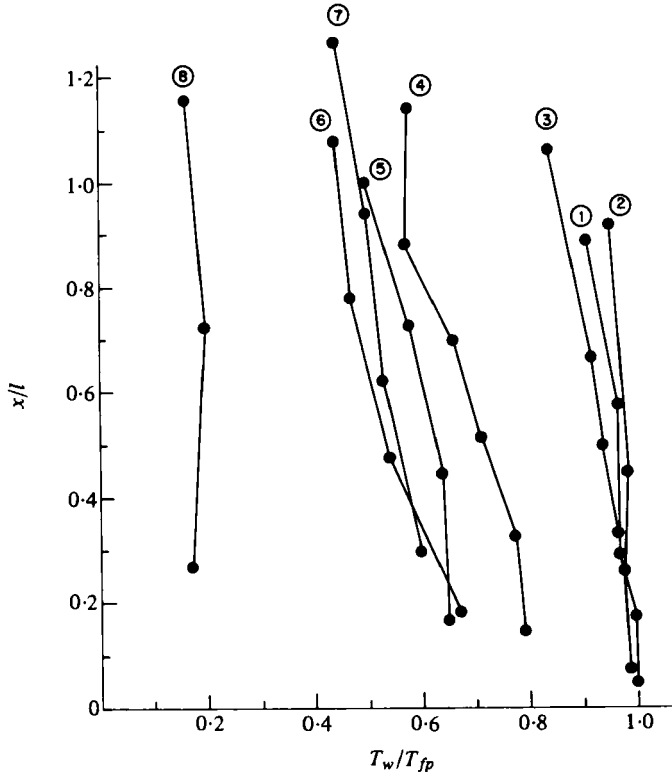$$\bar{M}_0 = 0\cdot76T_d^{1\cdot6} \times 10^{-3}\,\text{mm}^{\frac{3}{4}}\,\text{s}^{-1}, \tag{8}$$

FIGURE 8. The vertical variation of $T_w/T_{fp}$ in the laminar region, where each circled number refers to an experiment listed in table 2.
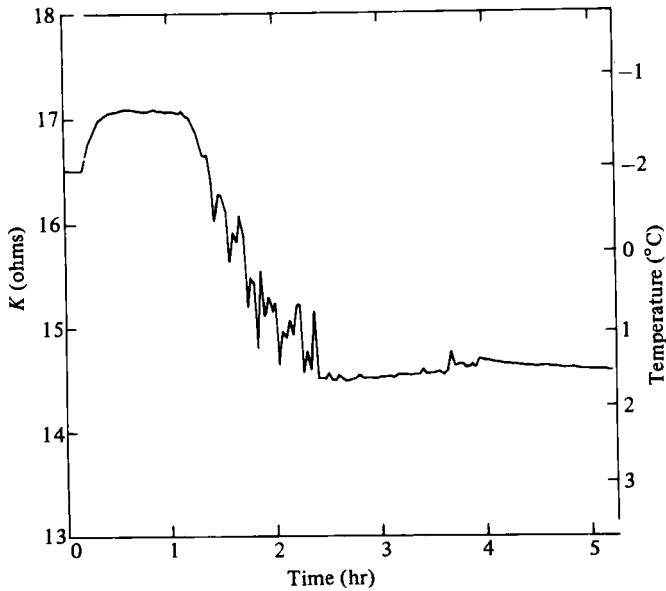


FIGURE 9. A representative thermistor record from the turbulent flow region. See text for further discussion.

| Experiment number | $T_\infty$ (°C) | $S_\infty$ (‰) | $T_d$ (deg) | $T_w$ (°C) | '$x$' (mm) | $M$ ($\mu$m s$^{-1}$) | $M_0 \times 10^3$ (mm$^{\frac{5}{4}}$ s$^{-1}$) | $\overline{M}_0 \times 10^3$ (mm$^{\frac{5}{4}}$ s$^{-1}$) |
|---|---|---|---|---|---|---|---|---|
| 1 | −0·10 | 29·9 | 1·53 | −1·27 | 360 | 0·58 | 2·5 | 2·5 |
| 2 | 1·55 | 29·0 | 3·13 | −0·92 | 70 | 1·22 | 3·5 | 3·7 |
|   |       |      |      |       | 200 | 1·02 | 3·8 |     |
| 3 | 2·00 | 30·0 | 3·63 | −0·76 | 510 | 1·57 | 7·5 | 7·7 |
|   |      |      |      |       | 610 | 1·56 | 7·8 |     |
|   |      |      |      |       | 940 | 1·40 | 7·8 |     |
| 4 | 2·20 | 30·0 | 3·83 | −0·76 | 115 | 1·87 | 6·1 | 6·8 |
|   |      |      |      |       | 250 | 1·89 | 7·5 |     |
| 5 | 2·66 | 34·4 | 4·55 | −0·74 | 180 | 2·15 | 7·9 | 8·7 |
|   |      |      |      |       | 330 | 2·23 | 9·5 |     |
| 6 | 3·42 | 30·0 | 5·05 | −0·59 | 470 | 2·47 | 11·5 | 11·0 |
|   |      |      |      |       | 520 | 2·23 | 10·6 |     |
|   |      |      |      |       | 760 | 2·09 | 11·0 |     |
| 7 | 6·85 | 33·95 | 8·71 | −0·59 | 220 | 6·29 | 24·2 | 25·2 |
|   |      |       |      |       | 360 | 5·99 | 26·1 |     |
| 8 | 10·85 | 34·1 | 12·72 | −0·06 | 240 | 9·58 | 37·7 | 39·0 |
|   |       |      |       |       | 370 | 9·16 | 40·2 |     |
| 9 | 16·31 | 35·2 | 18·24 | −0·02 | 290 | 14·27 | 58·9 | 58·9 |

TABLE 3. Far-field conditions, ice-water interface temperatures and melt rates for the turbulent flow experiments.

while for $9 \leqslant T_d \leqslant 20$ deg,

$$\overline{M}_0 = (3\cdot55T_d - 5\cdot89) \times 10^{-3} \text{ mm}^{\frac{5}{4}} \text{ s}^{-1}. \tag{9}$$

The change in melt rate at $T_d \simeq 9$ deg results from the buoyancy and heat-transfer dependence on $\Delta S = S_\infty - S_w$ and $\Delta T = T_\infty - T_w$. To explain this change, we assume that the melt rate is proportional to the product of $\Delta T$ and a transfer coefficient that is an increasing function of the net buoyancy. For $T_d < 9$ deg, figure 10 shows that both $\Delta T$ and $\Delta S$ increase nearly linearly with increasing $T_d$; because salinity primarily determines the density, the buoyancy also increases with $T_d$. Therefore the combination of an increase in both $\Delta T$ and net buoyancy gives a melt rate that depends nonlinearly on $T_d$. For $T_d > 9$ deg, since $S_w$ has approached zero, the net buoyancy remains almost constant but $\Delta T$ continues to increase with increasing $T_d$. Therefore, the melt rate increases linearly with $T_d$. For $T_d > 20$ deg the thermal effect on density overwhelms the saline effect and produces the high-temperature flow reversal discussed in the next section.

### 4.3. *The high temperature flow reversal*

For $T_d > 20$ deg our experiments show that the flow reverses; the flow consists of a laminar bidirectional boundary layer at the *top* of the ice above a downward flowing turbulent boundary layer. In addition, the ice ablates smoothly in the laminar region, but irregularly in the turbulent region where cusps appear in the ice surface.

To investigate the flow at temperatures near $T_d = 20$ deg, we performed two qualitative experiments close to the predicted flow reversal line derived below in §7. In both cases the flow was unsteady with both up and down flow; generally the flow consisted of an inner upward-flowing layer near the ice inside of an intermittent downflow. In one case, the melting cooled the tank sufficiently so that the flow settled
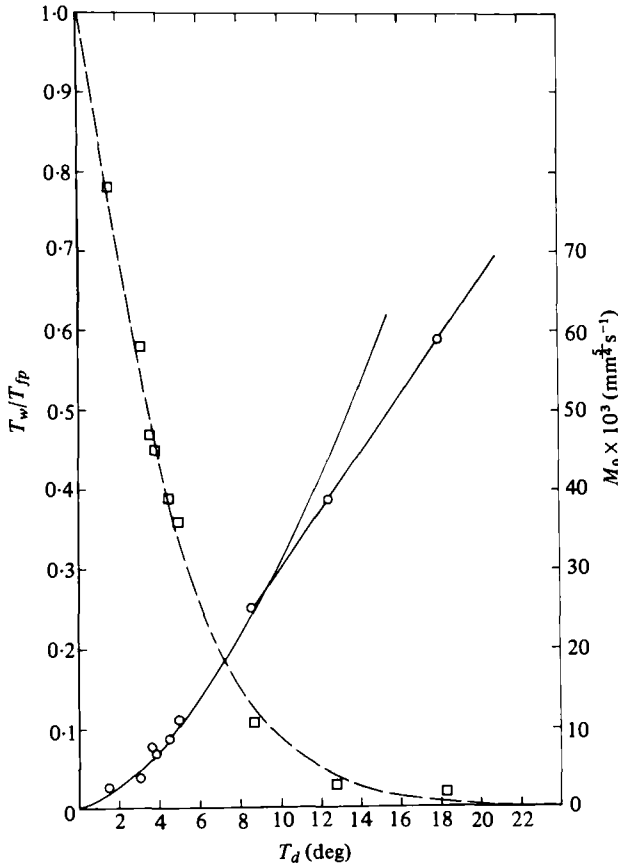
FIGURE 10. Experimental values of $T_w/T_{fp}$ ($\square$) and $\overline{M}_0$ ($\bigcirc$) for the turbulent flow.

into the pattern observed for $T_d < 20$ deg. In the other case, $T_d$ was large enough that cusps appeared on the ice and a flow reversal occurred.

We performed two experiments at $T_d > 20$ deg, $T_d = 27 \cdot 7$ deg, and $26 \cdot 6$ deg; figure 11 is a sketch of the observed flow and the resulting ice shape. At the top of the ice, we found a 60 mm long laminar bidirectional layer with a 1–2 min thick upward inner layer inside of a 10–20 mm thick downward outer layer. The ice adjacent to this flow melted smoothly. Below this laminar flow we observed a 20–30 mm thick turbulent downward-flowing boundary layer that grew in thickness; the ice adjacent to this layer melted irregularly to produce cusps. Figure 12 shows the smooth ice at the top and the cusped region below; at the beginning of the experiment, this piece of ice was planed smooth; we took the photograph after the ice had been submerged for 23 minutes in salt water at 24·8 °C and 33·6‰, or $T_d = 26 \cdot 6$ deg.

The vertical lengths of the cusps grew longer as the experiment progressed. Initially, well-ordered cusps form within 12 min from the beginning of an experiment with a vertical length of 10 mm and a cross-stream length of 20 mm. After 30 min the cusps are disorganized with equal vertical and cross-stream lengths of approximately 30 mm. In both cases the cusps were larger where the boundary layer is thicker. The depth of the cusps also increased with time to a final depth of approximately 5 mm.
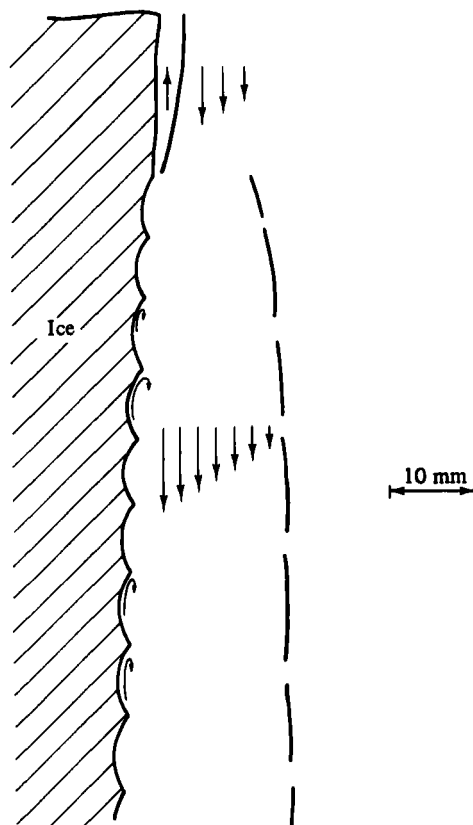
FIGURE 11. A sketch of the flow observed for $T_d > 25$ deg.

Dye injections into the cusps show the presence of a back eddy in the cusps as illustrated by the small arrows in figure 11. The dye flowed upward and then outward at the crest of the cusp, then downward in the mean flow. Occasionally, some dye flowed over a crest and into a higher cusp before being swept downward. We observed no net upward flow adjacent to the ice in the turbulent portion of the boundary layer.

To estimate the melt rates in these experiments, we measured the ice thickness before and after the experiment. Because of the irregular shape of the ice these measurements give only an estimate of the melt rate. The melt rate for $T_\infty = 24\cdot8$ °C and $S_\infty = 33\cdot6$‰, $T_d = 26\cdot6$ deg, was $48\cdot6\,\mu\mathrm{m\,s^{-1}}$; the melt rate for $T_\infty = 26\cdot0$ °C and $S_\infty = 31\cdot0$‰, $T_d = 27\cdot7$ deg, was $31\cdot1\,\mu\mathrm{m\,s^{-1}}$. For the second experiment, the values of $T_w$ were all equal to $-0\cdot02$ °C so that nearly fresh water is found at the wall.

## 5. The governing equations

To investigate the oceanographically interesting case of the turbulent upward flow, we next numerically solve the governing equations in similarity form. The governing equations consist of the mass conservation equation, the momentum equation, the two diffusion equations for salt and heat, and the equation of state from Gebhart & Mollendorf (1977). For our case, these equations take the following form: First, incompressibility gives
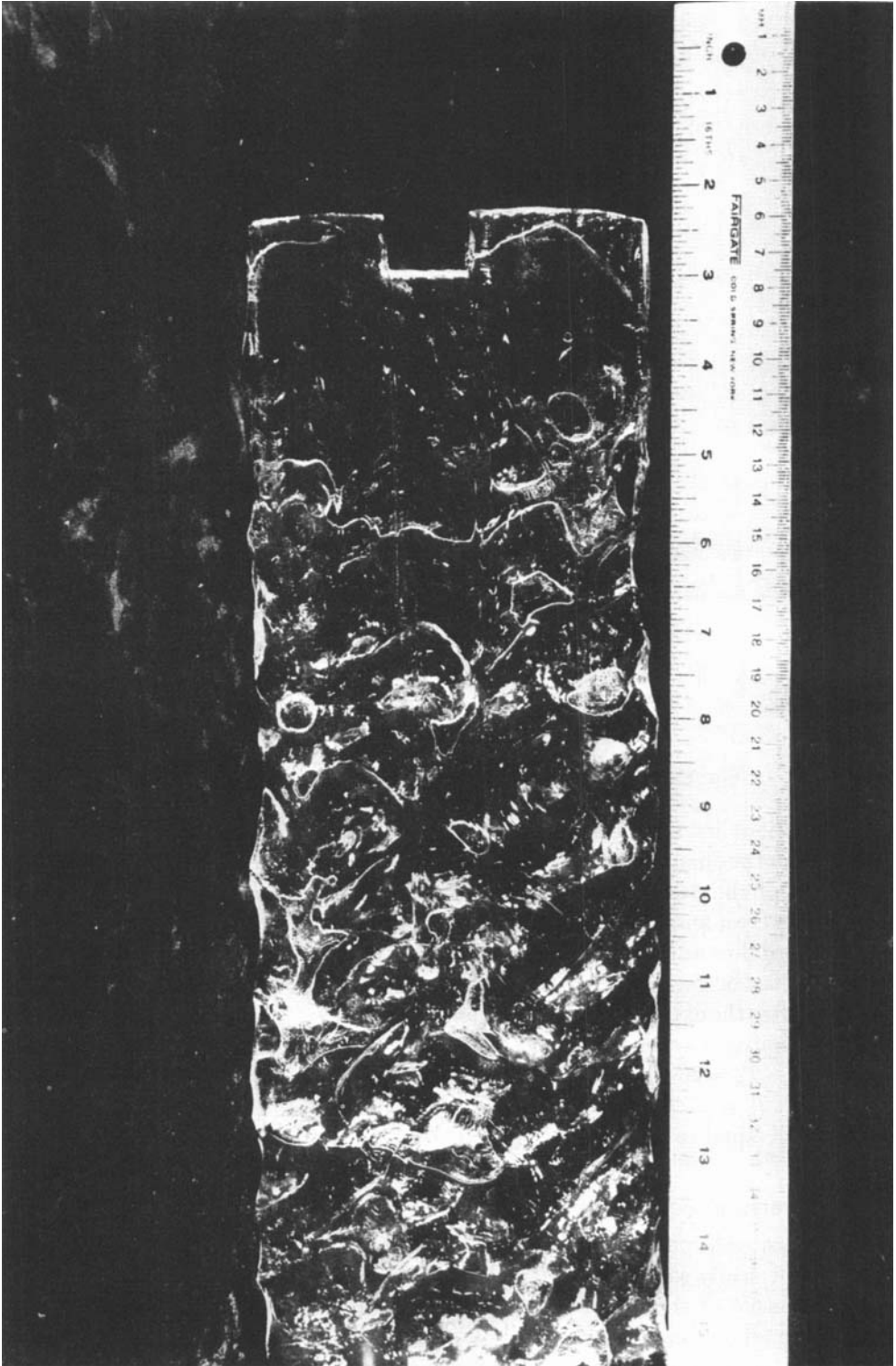
$$\nabla \cdot \bar{\mathbf{u}} = 0. \tag{10}$$

FIGURE 12. Ice shape after melting for 23 min, $T_\infty = 24\cdot8$ °C, $S_\infty = 33\cdot6$ ‰.
Note smooth upper portion and cusped lower portion.

Secondly, following Tennekes & Lumley (1972), the mean momentum equations of a Boussinesq fluid in two dimensions with $x$ vertical and $y$ normal to the ice are

$$\frac{\partial u}{\partial t}+u\frac{\partial u}{\partial x}+v\frac{\partial u}{\partial y} = -\frac{1}{\rho}\frac{\partial p}{\partial x}+\frac{(\rho_0+\tilde{\rho})}{\rho_0}g+\nu\left(\frac{\partial^2 u}{\partial x^2}+\frac{\partial^2 u}{\partial y^2}\right)-\left(\frac{\partial}{\partial x}\overline{u'u'}+\frac{\partial}{\partial y}\overline{u'v'}\right), \quad (11a)$$

$$\frac{\partial v}{\partial t}+u\frac{\partial v}{\partial x}+v\frac{\partial v}{\partial y} = -\frac{1}{\rho}\frac{\partial p}{\partial y}+\nu\left(\frac{\partial^2 v}{\partial x^2}+\frac{\partial^2 v}{\partial y^2}\right)-\left(\frac{\partial}{\partial x}\overline{v'u'}+\frac{\partial}{\partial y}\overline{v'v'}\right), \quad (11b)$$

where $u$, $v$ are mean velocity components; $u'$, $v'$ are turbulent velocity fluctuations; $p$ is pressure; $\rho_0$ is the undisturbed density; and $\tilde{\rho} = \tilde{\rho}(S, T)$ is the density perturbation due to changes in the mean salinity and temperature. Thirdly, because the salt and heat diffusion equations have the same form, we only write the salt diffusion equation as

$$\frac{\partial S}{\partial t}+u\frac{\partial S}{\partial x}+v\frac{\partial S}{\partial y} = D\left[\frac{\partial^2 S}{\partial x^2}+\frac{\partial^2 S}{\partial y^2}\right]-\left[\frac{\partial}{\partial x}(\overline{u'S'})+\frac{\partial}{\partial y}(\overline{v'S'})\right] \quad (11c)$$

where primes denote turbulent fluctuations.

To simplify equations (11a–c), we first neglect the normal turbulent stresses as these terms transport little mean momentum. Then, because our laboratory observations show that the ratio of the flow thickness to the ice block length is of order $10^{-2}$, we make the boundary-layer approximation. Next, we model the turbulent transport processes with an eddy diffusivity that varies with both position in the boundary layer and the thermal driving. In this simple model we assume that the diffusivities of momentum, heat and salt are equal because turbulence is a flow property that acts to transport quantities equally. The model in this case is

$$\overline{u'v'} = A\frac{\partial u}{\partial y}, \quad \overline{v'S'} = A\frac{\partial S}{\partial y}, \quad \overline{v'T'} = A\frac{\partial T}{\partial y}, \quad (12a, b, c)$$

where the eddy diffusivity $A$ is a function of $x$, $y$ and $T_d$.

Fourthly, because our laboratory observations show that the melt rate and the mean flow adjacent to the ice are steady, we transform (11) to a moving co-ordinate system fixed to the ice–water interface to remove the time dependence. With the interface position given as $y_i = \sigma(x, t)$, we write

$$y = \sigma(x, t)+y_r, \quad v = v_r+\frac{\partial\sigma}{\partial t}, \quad (13a, b)$$

where $y_r$ and $v_r$ are respectively the $y$ co-ordinate and the $y$ velocity in the moving frame. With the substitution of (12) and (13) into (11), the governing equations with the subscript $r$ dropped for clarity become

$$\frac{\partial u}{\partial x}+\frac{\partial v}{\partial y} = 0, \quad (14a)$$

$$u\frac{\partial u}{\partial x}+v\frac{\partial u}{\partial y} = \frac{-\tilde{\rho}}{\rho_0}g+\frac{\partial}{\partial y}\left[(\nu+A)\frac{\partial u}{\partial y}\right], \quad (14b)$$

$$u\frac{\partial T}{\partial x}+v\frac{\partial T}{\partial y} = \frac{\partial}{\partial y}\left[(\kappa+A)\frac{\partial T}{\partial y}\right] \quad (14c)$$

and

$$u\frac{\partial S}{\partial x}+v\frac{\partial S}{\partial y} = \frac{\partial}{\partial y}\left[(D+A)\frac{\partial S}{\partial y}\right]. \quad (14d)$$

The boundary conditions for a melting or freezing liquid–solid interface follow from the application of the no-slip condition, the freezing condition, and the conservation of mass, heat and salt. For a curved interface, LaPadula & Mueller (1970) and Josberger (1979) derive the boundary conditions. In the present study, because the surface in the turbulent region is almost flat, we use only the following five one-dimensional boundary conditions, each of which applies at $y = 0$.

First, the no-slip condition is

$$u = 0. \tag{15}$$

Secondly, following Frank (1950) and Sekerka (1973, §15.2) $T_w$ and $S_w$ must lie on the freezing curve (1), or

$$T_w = -mS_w, \tag{16}$$

and thirdly, the salt flux condition is that

$$-S_w \frac{\rho_i}{\rho_w} \frac{\partial \sigma}{\partial t} = D \frac{\partial S}{\partial y}. \tag{17}$$

Fourthly, from Carslaw & Jaeger (1959) the heat flux at the interface, on the assumption of no heat conduction in the ice interior, is

$$\kappa \frac{\partial T}{\partial y} = -L\rho_i \frac{\partial \sigma}{\partial t} \quad \text{at} \quad y = 0, \tag{18}$$

where $L = 3\cdot3 \times 10^5 \, \text{J kg}^{-1}$ and $\rho_i = 920 \, \text{kg m}^{-3}$. Finally, the mass flux normal to the ice must equal the flux introduced by the melting, so that

$$v(0) = -\frac{\rho_i}{\rho_w} \frac{\partial \sigma}{\partial t}. \tag{19}$$

Next, the boundary conditions at infinity are

$$u = 0, \quad S = S_\infty, \tag{20a, b}$$

and

$$T = T_\infty \quad \text{at} \quad y = \infty. \tag{20c}$$

To simplify further the governing equations we introduce a stream function defined as

$$u = \frac{\partial \psi}{\partial y} \quad \text{and} \quad v = -\frac{\partial \psi}{\partial x}, \tag{21}$$

and replace $T$ and $S$ with normalized non-dimensional variables given by

$$\theta = \frac{T - T_\infty}{T_w - T_\infty}, \quad \phi = \frac{S - S_\infty}{S_w - S_\infty}. \tag{22}$$

With (21) and (22), the following similarity transformation reduces equations (14a–d) to ordinary differential equations:

$$\psi = ax^p f(\eta), \quad A = x^r A_s(\eta, T_d), \tag{23a, b}$$

$$\phi = \phi(\eta), \quad \theta = \theta(\eta), \quad \eta = \frac{by}{x^q}, \tag{23c, d, e}$$

where $f$, $A_s$, $\phi$ and $\theta$ are unknown functions, $\eta$ is the similarity variable, and $a$, $b$, $p$,

$q$ and $r$ are unknown constants. Because our laboratory observations show that $S_w$ and $T_w$ have no measurable $x$-variation, we assume $\phi$ and $\theta$ are functions of $\eta$ only.

Substitution of (21)–(23) into (14$b$) with the requirement that the resultant equation be independent of $\dot{x}$, gives

$$p = \tfrac{3}{4}, \quad q = \tfrac{1}{4} \quad \text{and} \quad r = 0. \tag{24}$$

Because $r = 0$, $A(x, y, T_d) = A_s(\eta, T_d)$, so that in the following we drop the subscript on $A_s$.

With $a$ and $b$ defined as

$$a = 4\nu b, \qquad b = \frac{-g(\rho_w - \rho_\infty)^{\frac{1}{4}}}{\rho_\infty 4\nu^2} \tag{25}$$

and $\rho_0 = \rho_\infty$, the transformed momentum equation becomes

$$2f'^2 - 3ff'' = \frac{\rho(\phi, \theta) - \rho_\infty}{\rho_w - \rho_\infty} + f'' \frac{A'}{\nu} + \left(1 + \frac{A}{\nu}\right) f''' \tag{26}$$

where primes denote differentiation with respect to $\eta$.

With the same substitutions, the diffusion equations (14$c$–$d$) become

$$-3f\phi' = \left(S_c + \frac{A}{\nu}\right)\phi'' + \phi' \frac{A'}{\nu} \tag{27a}$$

and

$$-3f\theta' = \left(P_r + \frac{A}{\nu}\right)\theta'' + \theta' \frac{A'}{\nu}. \tag{27b}$$

With $\phi \equiv 0$ and $A \equiv 0$, equations (26) and (27) reduce to the laminar equations for convection adjacent to a heated wall given by Ostrach (1953).

Transformation of the far-field boundary conditions gives

$$f' = 0, \quad \phi = 0, \quad \text{and} \quad \theta = 0 \quad \text{at} \quad \eta = \infty. \tag{28}$$

At the ice–water interface the no-slip condition becomes

$$f'(0) = 0 \quad \text{at} \quad \eta = 0; \tag{29}$$

and the freezing curve condition becomes

$$\phi = \theta = 1 \quad \text{at} \quad \eta = 0. \tag{30}$$

To complete transformation of the wall boundary conditions (17)–(19), we take

$$\frac{\partial \sigma}{\partial t} = M_0(T_d) x^{-\frac{1}{4}} \tag{31}$$

where $M_0$ is specified by the laboratory data of equations (8)–(9). With equation (31), the boundary conditions (17)–(19) become

$$\phi'(0) = -\frac{S_w \rho_i M_0}{D\rho_w(S_w - S_\infty)b}, \tag{32a}$$

$$\theta'(0) = -\frac{L\rho_i M_0}{\kappa(T_w - T_\infty)b}, \tag{32b}$$

$$f(0) = \frac{\rho_i}{\rho_w} \frac{M_0}{3\nu b}, \quad \text{at} \quad \eta = 0. \tag{32c}$$

## 6. The turbulent model

To model the turbulent transport processes we follow Townsend's (1976) discussion of the turbulent structure of a wall jet. For a wall jet, the position of the mean maximum upward velocity divides the flow into an inner and an outer region. In the inner region the turbulence has the characteristics of wall turbulence next to a smooth wall as originally proposed by Prandtl. The inner region further divides into a viscous sublayer where molecular transport processes dominate and a region where the eddy diffusivity increases linearly with distance from the wall. In the outer region, the turbulence has the characteristics of free turbulence; the eddy diffusivity is constant.

Mathematically, we formulate this model as

$$A(\eta, T_d) = 0 \quad \text{for} \quad 0 \leqslant \eta \leqslant \Delta\eta, \tag{33a}$$

$$A(\eta, T_d) = A_0(T_d)\left[1 - \operatorname{sech}\left(\gamma(\eta - \Delta\eta)\right)\right] \quad \text{for} \quad \eta \geqslant \Delta\eta, \tag{33b}$$

where the viscous sublayer thickness is $\Delta\eta$ and $\gamma$ is a shape factor. We also assume that $A_0$ contains all the $T_d$-dependence.

In this model at a given $T_d$, $A$ remains constant as $\eta$ increases beyond the boundary-layer thickness instead of decreasing. However, the solution to the equations remains unaffected because the gradients of momentum, heat and salt are zero outside the boundary layer and therefore the diffusive fluxes are zero regardless of the value of the diffusion coefficient. Keeping $A$ large outside the boundary layer simplifies the numerical integration of the equations by allowing the use of a large integration step size which speeds the computations. Many investigators have used similar schemes successfully (cf. Betchov & Criminale 1964).

### 6.1. *The numerical scheme*

To solve the seventh-order nonlinear governing equations with implicit boundary conditions we used the quasi-linearization scheme of Radbill & McCue (1970), which Josberger (1979) describes in detail. In our case, specification of the boundary conditions at $\eta = 0$ and $\eta = \infty$ gives a two-point boundary-value problem, where we apply the $\eta = \infty$ boundary conditions at $\eta = 20$, a distance which corresponds to approximately three times the observed boundary-layer thickness. Numerical iteration to a solution continues until the difference between successive iterations is less than $5 \times 10^{-3}$. To check the sensitivity of the solution to the convergence parameter we ran duplicate cases with the convergence parameter equal to $5 \times 10^{-3}$ and $10^{-3}$ and found no discernible differences between the solutions.

### 6.2. *The numerical results*

The numerical results show that both blowing and opposing buoyancy forces must be included in the analysis to model adequately the flow. Josberger (1979) contains the computer tabulations for $0 \leqslant \eta \leqslant 20$ and $2 \leqslant T_d \leqslant 12$ deg; here we present only the graphical results. We base our numerical calculations on the values of $\phi'(0)$, $\theta'(0)$, $f'(0)$, $a$, and $b$ which we list in table 4 for different values of $T_d$ and which we derived from the smoothed laboratory data. To evaluate the turbulent parameters at the appropriate $T_d$'s, we varied $A$, $\gamma$, and $\Delta\eta$ until the computer-generated values of $\phi'(0)$, $\theta'(0)$, and $f'(0)$ equalled the laboratory values. We also required that the

| $T_d$ (deg) | $\phi'_{\text{lab}}(0)$ | $\theta'_{\text{lab}}(0)$ | $f'_{\text{lab}}(0) \times 10^{-3}$ | $a$ $(\text{mm}^{\frac{1}{4}}\,\text{s}^{-1})$ | $b$ $(\text{mm}^{-\frac{1}{4}})$ |
|---|---|---|---|---|---|
| 2 | $-5\cdot02$ | $-0\cdot556$ | $-0\cdot26$ | $11\cdot0$ | $1\cdot53$ |
| 4 | $-4\cdot67$ | $-0\cdot720$ | $-0\cdot68$ | $12\cdot8$ | $1\cdot78$ |
| 6 | $-3\cdot83$ | $-0\cdot837$ | $-1\cdot24$ | $13\cdot7$ | $1\cdot90$ |
| 8 | $-2\cdot93$ | $-0\cdot937$ | $-1\cdot92$ | $14\cdot2$ | $1\cdot97$ |
| 10 | $-2\cdot04$ | $-0\cdot982$ | $-2\cdot59$ | $14\cdot4$ | $2\cdot00$ |
| 12 | $-1\cdot33$ | $-0\cdot989$ | $-3\cdot22$ | $14\cdot5$ | $2\cdot02$ |

TABLE 4. Values of $\phi'_{\text{lab}}(0)$, $\theta'_{\text{lab}}(0)$, $f'_{\text{lab}}(0)$, $a$ and $b$ computed from the smoothed laboratory data.

solutions had to yield only upward flow and give a boundary-layer thickness of approximately 10 $\eta$ units.

At $T_d = 4$ deg with $\gamma = 1\cdot5$, we found that variations of $A$ have a larger effect on $\theta'(0)$ than on $\phi'(0)$ while the opposite holds true for variations of $\Delta\eta$; this results from the large Lewis number. The relatively large $\kappa$ allows the cooling to diffuse through the laminar region into the turbulent region where the turbulence has a large effect on the heat transfer. The relatively small $D$ contains the saline anomaly close to the ice where changes in $\Delta\eta$ greatly effect the salt distribution. For the model at $T_d = 4$ deg we chose $A_0$ and $\Delta\eta$ equal to $0\cdot28\ \text{mm}^2\text{s}^{-1}$ and $0\cdot078$, respectively, because these values gave an average error in the salinity and temperature gradients of less than 5 %.

To determine the dependence on $T_d$ of $A_0$, we assume it depends on an unknown power of the non-dimensional buoyancy, so that

$$A_0 = C_0 \left( \frac{\rho_\infty - \rho_w}{\rho_\infty - \rho_f} \right)^n \tag{34}$$

where $\rho_w$ is the interfacial water density, $\rho_f$ is the freshwater density, $n$ is an undetermined exponent and $C_0$ is a constant. To write (34) in terms of $T_d$, we assume $\rho$ is a linear function of $S$. Then using equation (17) and (16), (34) becomes

$$A_0 = C_0 \left[ \tanh (0\cdot15 T_d) \right]^n. \tag{35}$$

To determine the coefficient $n$, we numerically solved the governing equations for $T_d$ equal to 2, 4 and 8 deg, and for three values of $n$: $1\cdot0$, $1\cdot5$ and $2\cdot0$, with $\Delta\eta$ held constant at $0\cdot09$. For each value of $n$, we adjusted $C_0$ to make $A_0$ at $T_d = 4$ deg equal to $0\cdot28\ \text{mm}^2\text{s}^{-1}$. Figure 13 compares the smoothed experimental data with the results from each set of calculations. The heavy solid line is the locus of experimental points. Each tick mark on this line represents the boundary conditions for consecutively increasing $T_d$, beginning at 2 deg at the lower right and ending at 12 deg at the upper left. The arbitrary division of melt rate dependence on $T_d$ given in (8) and (9) produces the kink at $T_d = 9$ deg. The symbols $\times$ and $\blacktriangle$ give the solutions for $n = 1\cdot0$ and $1\cdot5$; both curves yield temperature and salinity gradients that are too low at $T_d = 8$ deg and too high at 2 deg. The final form of the turbulent model is

$$\left. \begin{array}{l} \gamma = 1\cdot5, \quad n = 2, \quad \Delta\eta = 0\cdot078, \\[4pt] \text{and} \qquad\qquad C_0 = 0\cdot922\ \text{mm}^2\text{s}^{-1}. \end{array} \right\} \tag{36}$$

The open circles in figure 13 denote the results of this model where the number inside of each circle is the $T_d$ for each computation. The magnitude of the eddy diffusivity,
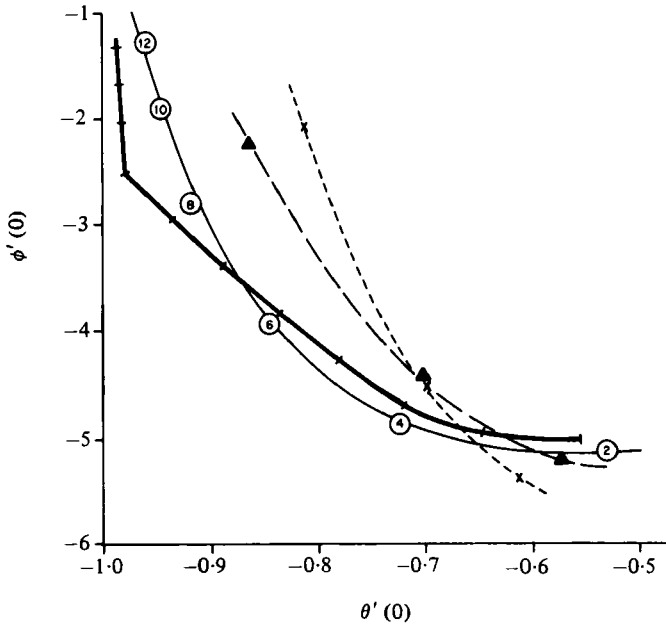
FIGURE 13. Locus of points from the smoothed laboratory data, and three models of the eddy diffusivity: $\bigcirc$, final eddy diffusivity model (equation (36)); $\times$, $n = 1\cdot0$; $\blacktriangle$, $n = 1\cdot5$.
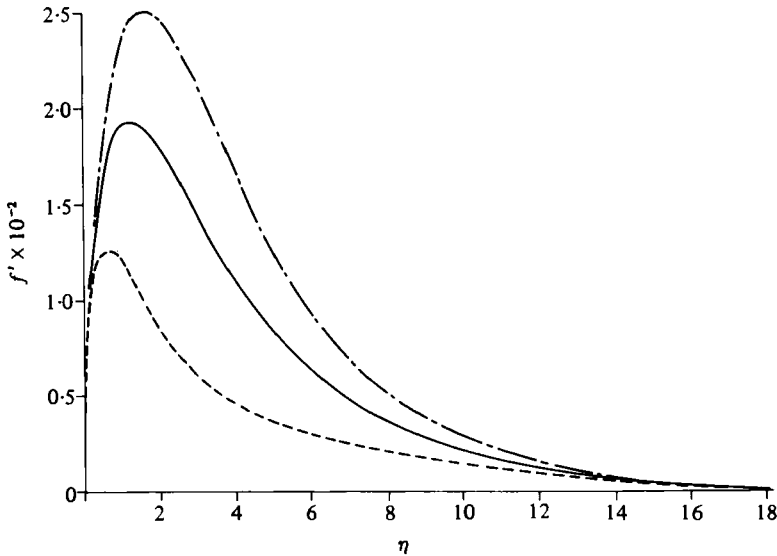


FIGURE 14. Computed profiles of $f'$ for: – – – –, $T_d = 2$ deg; ——, $T_d = 4$ deg; – – –, $T_d = 8$ deg.

$C_0$, is approximately one half the value of the laminar viscosity which demonstrates the weak nature of the turbulence.

In this model, we fix $\gamma$ at $1\cdot5$ to satisfy the condition that $A$ reaches its maximum value in the region of maximum upward velocity. To illustrate, figure 14 gives the $f'$ profiles using (36) for $T_d = 2$, 4 and 8 deg; we omit the profile for $T_d = 12$ deg because it is nearly identical with that at 8 deg.

| $T_d$ (deg) | $f'_{max} \times 10^2$ | | | $f(\infty) \times 10^2$ | | | $F(\infty)$ (mm$^{\frac{4}{3}}$ s$^{-1}$) |
|---|---|---|---|---|---|---|---|
| | $\rho(S, T)$ | No blowing | $\rho(S)$ | $\rho(S, T)$ | No blowing | $\rho(S)$ | $\rho(S, T)$ |
| 2 | 1·26 | 1·13 | 1·45 | 5·50 | 4·30 | 8·04 | 0·60 |
| 4 | 1·93 | 1·55 | 2·31 | 10·8 | 8·60 | 11·90 | 1·38 |
| 6 | 2·30 | — | 2·88 | 12·3 | — | 14·7 | 1·69 |
| 8 | 2·50 | 1·26 | 3·39 | 13·6 | 3·34 | 17·6 | 1·93 |
| 10 | 2·57 | — | 3·69 | 13·8 | — | 18·2 | 1·99 |
| 12 | 2·52 | — | 4·02 | 13·2 | — | 19·7 | 1·91 |

TABLE 5. The turbulent-flow transport properties for three cases: opposed buoyancy forces with blowing, $\rho(S, T)$; opposed buoyancy forces without blowing; and density as a function of $S$ only, $\rho(S)$.

The figure shows that the maximum velocity occurs for $0\cdot7 \leqslant \eta \leqslant 2\cdot0$; for $\gamma = 1\cdot5$, $A(\eta)$ attains 90 % of its maximum value in the required region for $T_d > 2$ deg. For $T_d < 2\cdot0$ deg, the position of the maximum velocity is so close to the wall that the eddy diffusivity has little direct effect on the momentum distribution. Hence, to simplify the calculations over the entire temperature range, we kept $\gamma$ constant for all $T_d$.

Figure 14 also displays the momentum boundary-layer characteristics. If we define the momentum boundary-layer thickness $\delta_m$ as that distance from the wall where $f'$ drops to 10 % of its maximum value, then figure 14 shows that $\delta_m$ is almost constant for all $T_d$. The figure also shows that $\delta_m$ equals approximately 11 $\eta$-units; this corresponds to approximately 25 mm which agrees with the laboratory observations. The constant value of $\delta_m$ for different $T_d$'s results from the values of $A_0$ which are always less than the molecular diffusivity; hence at all $T_d$, $\nu$ determines $\delta_m$.

Next, table 5 lists for both the present case labelled $\rho(S, T)$ and for two other cases discussed in the next section, certain flow properties as a function of $T_d$. For these cases, the table lists the maximum value of $f'$, $f'_{max}$, and the non-dimensional upward mass transport, $f(\infty)$. The last column also gives the dimensional transport $F(\infty)$. For the present case, columns 2 and 5 show that both $f'_{max}$ and $f(\infty)$ increase almost linearly for $2 \leqslant T_d \leqslant 8$ deg; this results from the almost linear increase in buoyant forcing for this range of $T_d$. Above $T_d = 8$ deg the buoyant forcing is almost constant so that $f'_{max}$ and $f(\infty)$ remain nearly constant except for a slight decrease at $T_d = 12$ deg which is the result of the increasing temperature effect on density at high temperature.

To compute the upward transport per unit width, (23 a) evaluated at $y = \infty$ gives

$$\Psi(\infty) = ax^{\frac{3}{4}} f(\infty) \equiv x^{\frac{3}{4}} F(\infty), \tag{37}$$

where $a$ is defined by (25) and given in table 4. The last column in table 5 lists $F(\infty)$, which figure 15 also plots for $0 \leqslant T_d \leqslant 4$ deg. The upward transport from a vertical wall in salt water of an arbitrary temperature and uniform salinity can be calculated from figure 15 and equation (37). For example, our laboratory case of a 0·5 m long boundary layer next to an ice slab 0·2 m wide in water at $T_d = 4$ deg, gives from (37) an upward transport of 0·13 m³ after 1 hour. Because the ice has two sides the upward transport must be doubled to give 0·25 m³. With our experimental tank having a cross-sectional area of 0·54 m², the convection after one hour replaces the water in the upper 0·4 m with cool dilute water. To counter the effects of this vigorous upflow, we used the
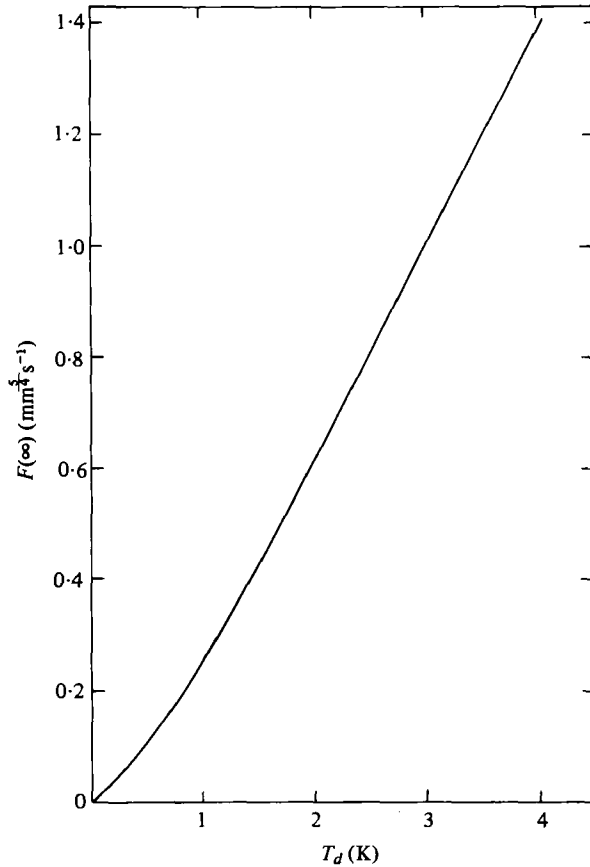
FIGURE 15. Computed values of $F(\infty)$ for $T_d \leqslant 4$ deg.

pumping and heating systems previously described to maintain uniform conditions. In a second example, we apply these results to an iceberg with a 100 m vertical length scale floating in water at $T_d = 2$ deg. The resulting upward transport is $294 \, \text{m}^2 \, \text{day}^{-1}$ per waterline metre. If the iceberg has a circumference of 1 km then the total upwelling equals $2 \cdot 9 \times 10^5 \, \text{m}^3 \, \text{day}^{-1}$. Hence, upwelling driven by melting icebergs as proposed by Neshyba (1977), may have a significant impact on the physical and biological oceanography of the polar seas.

Next, figure 16 gives the profiles of $\phi$ and $\theta$ for a thermal driving of 4, 8 and 12 deg. The two most important features are the difference between $\delta_S$ and $\delta_T$ and the thickening of each boundary layer as the thermal driving increases. The difference in the boundary-layer thicknesses results from the low turbulence levels and the large Lewis number. The laminar region adjacent to the ice and the small value of $D$ act to contain 95 % of the saline anomaly to within 1 $\eta$ unit of the ice wall, with the remaining 5 % spread out by the eddy diffusivity 4 or 5 $\eta$. Even though $\delta_T > \delta_S$, the large effect of salinity on density and the combined diffusion of upward momentum and saline anomaly out from the wall overwhelm any downward thermally produced momentum.
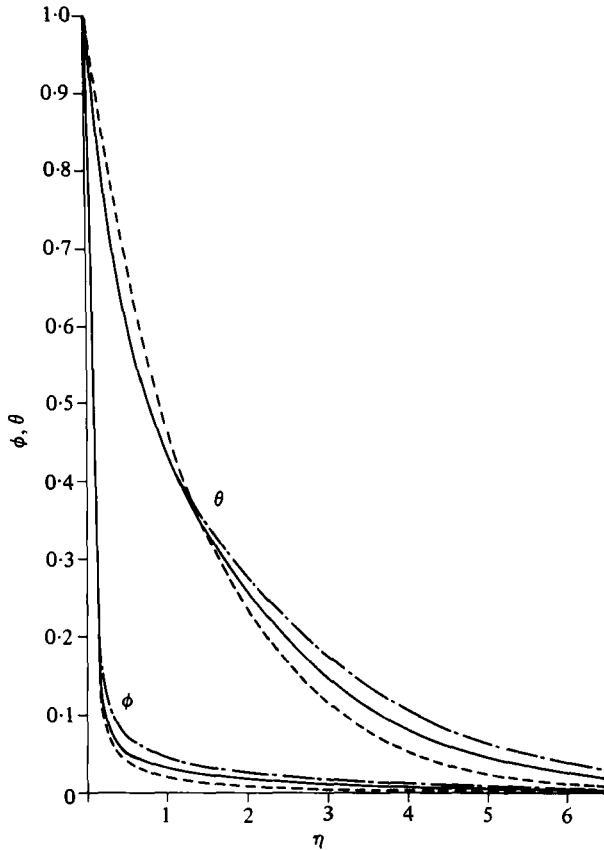
FIGURE 16. Computed profiles of $\phi$ and $\theta$ for: – – – –, $T_d = 4$ deg; ——, $T_d = 8$ deg; – — –, $T_d = 12$ deg.

### 6.3. *The effect of neglecting blowing and opposing buoyancy forces*

To determine the effect of blowing at the ice–water interface we set the velocity normal to the ice to zero so that (32c) becomes $f(0) = 0$ at $\eta = 0$ and resolve the equations using identical turbulence parameters. On figure 17 the circled numbers and the broken lines show the effect of no blowing on $\phi'(0)$ and $\theta'(0)$; while the heavy solid line shows the results of the calculations with blowing at the interface. Comparison of the two cases shows for the no-blowing case that as $T_d$ increases, $\phi'(0)$ and $\theta'(0)$ become more negative corresponding to both higher salt and heat fluxes to the ice. Table 5, which lists in columns 3 and 6 the values of $f'_{max}$ and $f(\infty)$ for the no-blowing case, shows that these values are much smaller and begin to decrease at lower values of $T_d$ than in the blowing case.

Secondly, to investigate the effect of opposing buoyancy forces on the model, we re-solve the governing equations with blowing and the same turbulent parameters but with the buoyancy determined by

$$\rho = \rho_\infty - \beta(S_\infty - S), \tag{38}$$

so that the density in only a function of $S$ and the temperature diffuses passively. In figure 17, the squares connected by the dashed line show the effect of opposing
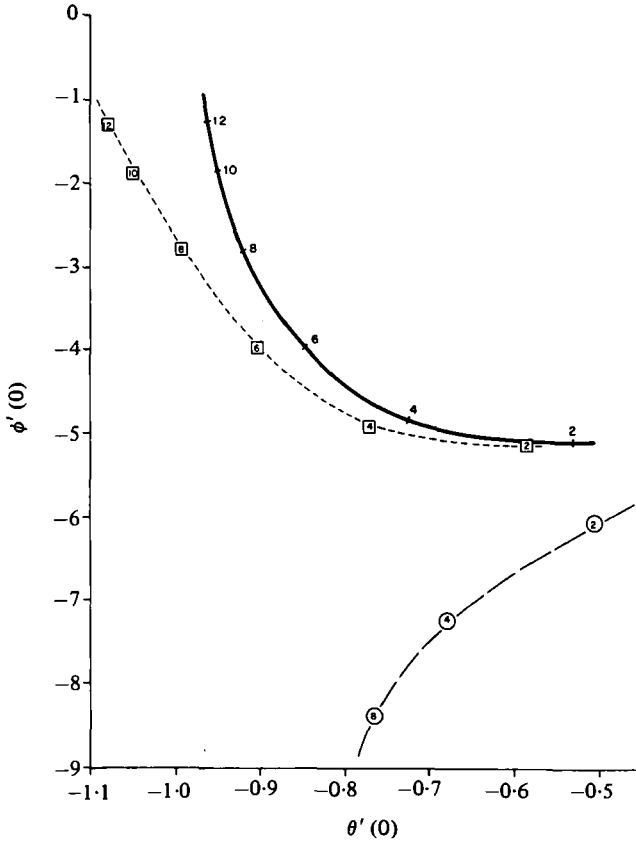
FIGURE 17. The effects of blowing and opposing buoyancy forces on $\phi'(0)$ and $\theta'(0)$ at various $T_d$: ——, results including both blowing and opposing buoyancy forces; — —, no blowing; – – – –, density only a function of salinity.

buoyancy forces on $\phi'(0)$ and $\theta'(0)$ for $T_d$ from 2 to 12 deg. Comparison of this curve to the heavy solid line shows that for the case of density as a function of salinity only, the values of $\phi'(0)$ remain almost constant while the values of $\theta'(0)$ become more negative corresponding to a higher heat flux to the ice. The values of $f'_{\max}$ and $f(\infty)$ listed in table 5 for this case show that neglecting of the temperature effect on density also increases the transport.

Returning to our original turbulent model, our calculations are valid for $T_d < 12$ deg; efforts to extend the model to $T_d = 14$ deg gave significant downward flow and values of $\phi'(0)$ and $\theta'(0)$ that disagreed with the smoothed laboratory data. Calculations at $T_d > 16$ deg failed to converge numerically. Because the observed flow reverses direction for $T_d > 20$ deg, one expects the numerical model based on upward flow to break down at high temperatures.

## 7. The high-temperature flow reversal

From the theoretical flow model, we next calculate the theoretical location in $T$–$S$ space of the flow reversal observed at $T_d > 20$ deg, then compare the results to those of Gade (1979) and Greisman (1979). In our case, we assume that the flow reverses when
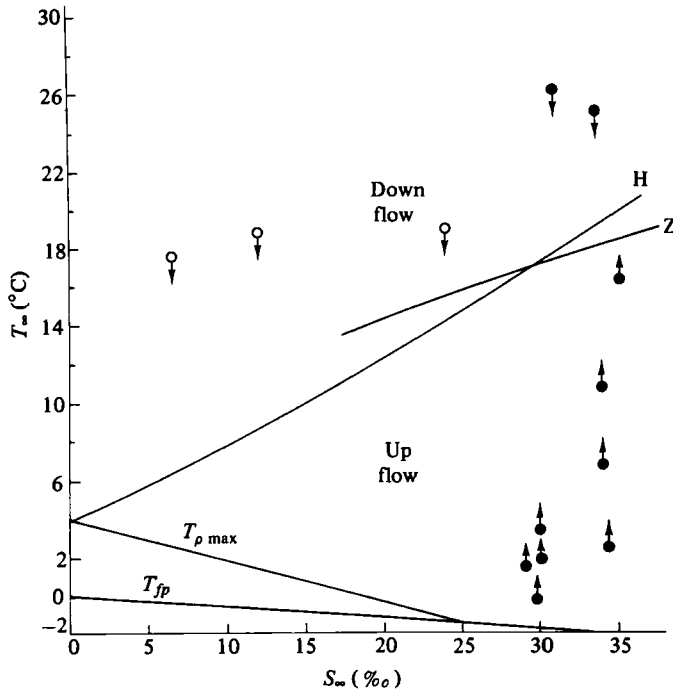
FIGURE 18. A $T$–$S$ diagram showing the location of the flow reversal line, $Z$, as predicted by equation (41) and as predicted by Gade (1979) and Greisman (1979), line $H$. The points give the far-field conditions; the arrows, the turbulent flow direction.

the buoyancy integrated across the boundary layer changes sign from positive to negative.

Hence, we define the net buoyancy $B$ as the density anomaly integrated across the boundary layer, where

$$B = \int_0^\infty \frac{[\rho_\infty - \rho(y)]}{\rho_\infty} \, dy. \tag{39}$$

In order to calculate from (39) the $T_\infty$ and $S_\infty$ that yield $B = 0$, we use the following linear equation of state:

$$\rho = \rho_\infty [1 + \beta(S - S_\infty) + \alpha(T - T_\infty)], \tag{40}$$

where $\alpha$ is evaluated at $S_\infty$ and $T_\infty$ to simplify the calculations and to give the maximum effect of temperature on density. Substitution of (22) into (40), use of the similarity transformation, and setting $S_w = T_w = 0$ which is valid for $T_\infty > 10\,°C$, gives

$$\beta S_\infty \frac{\displaystyle\int_0^\infty \phi \, d\eta}{\displaystyle\int_0^\infty \theta \, d\eta} = -\alpha(S_\infty, T_\infty) \, T_\infty. \tag{41}$$

From our flow model at the highest valid thermal driving, $T_d = 12\,\mathrm{deg}$, we evaluate the ratio of the two integrals on the left-hand side of (41) as equal to 0·157. This simplification yields for a particular $S_\infty$ a transcendental equation for $T_\infty$.

An iterative technique solved (41) for $S_\infty \leqslant 40\%_0$; figure 18 shows the position of the zero net buoyancy curve, labelled $Z$, on a $T$–$S$ diagram. For far-field conditions that lie below $Z$, the net buoyancy is upward; for far-field conditions above $Z$, the net buoyancy is downward. Because we assume $S_w = T_w = 0$ and because the linear equation of state becomes increasingly erroneous at low temperatures, we only plot $Z$ for $T_\infty > 10\,^\circ\mathrm{C}$.

Secondly, the curve labelled $H$ on figure 18 shows the location of the flow reversal line predicted by both Gade (1979) and Greisman (1979). To predict this line they allow one gram of ice to melt in a given mass of salt water then calculate the position on a $T$–$S$ diagram of the zero density change. In their model, the cooling and dilution effects are equally mixed in the final water volume, while in our dynamic model, integration of the buoyancy across the flow retains the effect of the different temperature and salinity distributions. This accounts for the difference between the curves $Z$ and $H$.

Thirdly, the points on figure 18 show the far-field conditions of the various experiments, where the arrow at each point indicates the turbulent flow direction. The dark circles are our experiments, the open circles were done jointly with Dr Herbert Huppert in our laboratory during September 1978. For the upward flowing cases the ice melted smoothly and there was a laminar bidirectional flow at the bottom of the ice. For the downward flowing cases cusps formed in the ice and there was a laminar bidirectional flow at the top of the ice. In all cases, the flow direction agrees with both theories.

The figure shows that the present data are insufficient to determine the validity of either model; a complete series of experiments over a wider range of temperatures and salinities would provide useful insight on the interaction of opposing buoyancy forces and the resulting flow direction.

## REFERENCES

BENDELL, M. S. & GEBHART, B. 1976 Heat transfer and ice melting in ambient water near its density extremum. *Int. J. Heat Mass Transfer* **19**, 1081–1087.

BETCHOV, R. & CRIMINALE, W. O. 1964 Oscillations of a turbulent flow. *Phys. Fluids* **7**, 1920–1926.

CALDWELL, D. R. 1974 The effect of pressure on thermal and Fickian diffusion of sodium chloride. *Deep-Sea Res.* **21**, 369–375.

CARSLAW, H. S. & JAEGER, J. C. 1959 *Conduction of Heat in Solids*, 2nd edn. Oxford University Press.

FRANK, F. C. 1950 Radially symmetric phase growth controlled by diffusion. *Proc. Roy. Soc.* A **201**, 586–599.

GADE, H. G. 1979 Melting of ice in sea water: a primitive model with application to the Antarctic ice shelf and icebergs. *J. Phys. Oceanog.* **9**, 189–198.

GEBHART, B. & MOLLENDORF, J. C. 1977 A new density relation for pure and saline water. *Deep-Sea Res.* **24**, 831–848.

GEBHART, B. & PERA, L. 1971 The nature of vertical natural convection flows resulting from the combined buoyancy effects of thermal and mass diffusion. *Int. J. Heat Mass Transfer* **14**, 2025–2050.

GREISMAN, P. 1979 On upwelling driven by the melt of ice shelves and tidewater glaciers. *Deep-Sea Res.* A **26**, 1051–1065.

HUPPERT, H. E. & TURNER, J. S. 1978 On melting icebergs. *Nature* **271**, 46–48.

JOSBERGER, E. G. 1979 Laminar and turbulent boundary layers adjacent to melting vertical ice walls in salt water. Ph.D. thesis, University of Washington, Seattle.

LaPADULA, C. A. & MUELLER, W. K. 1970 The effect of buoyancy on the formation of a solid deposit freezing onto a vertical surface. *Int. J. Heat Mass Transfer* **13**, 13–26.

NESHYBA, S. 1977 Upwelling by icebergs. *Nature* **267**, 507–508.

NEUMANN, G. & PIERSON, W. J. 1966 *Principles of Physical Oceanography*. Prentice Hall.

OSTRACH, S. 1953 An analysis of laminar free-convection flow and heat transfer about a flat plate parallel to the direction of the generating body force. *N.A.C.A. Tech. Rep.* 1111, pp. 1–17.

RADBILL, J. R. & McCUE, G. A. 1970 *Quasilinearization and Nonlinear Problems in Fluid and Orbital Mechanics*. Elsevier.

SANDSTROM, W. J. 1919 The hydrodynamics of the Canadian Atlantic waters. In *Canadian Fisheries Expedition, 1914–1915, in the Gulf of St. Lawrence and Atlantic Waters of Canada* (ed. J. Hjort), Department of the Naval Service, Ottawa, Canada. (U. W. Fisheries Library no. 591.92C161c.)

SCHLICHTING, H. 1960 *Boundary Layer Theory*, 4th edn. McGraw-Hill.

SEKERKA, R. F. 1973 Morphological Instability. In *Crystal Growth: An Introduction* (ed. P. Hartman), pp. 403–443. North Holland.

TENNEKES, H. & LUMLEY, J. L. 1972 *A First Course in Turbulence*. Massachusetts Institute of Technology Press.

TOWNSEND, A. A. 1976 *The Structure of Turbulent Shear Flow*, 2nd edn. Cambridge University Press.

TURNER, J. S. 1973 *Buoyancy Effects in Fluids*. Cambridge University Press.

WEAST, R. L. 1977 *Handbook of Chemistry and Physics*, 57th edn, p. D–252. Cleveland: Chemical Rubber Company Press.